Lensing of gravitational waves: Efficient wave-optics methods and validation with symmetric lenses

Giovanni Tambalo[*],[1,*] Miguel Zumalacárregui[*],[1,†] Liang Dai[*],[2,‡] and Mark Ho-Yeuk Cheung[3,§]

[1]*Max Planck Institute for Gravitational Physics (Albert Einstein Institute),*
Am Mühlenberg 1, D-14476 Potsdam-Golm, Germany
[2]*University of California at Berkeley, Berkeley, California 94720, USA*
[3]*William H. Miller III Department of Physics and Astronomy, Johns Hopkins University,*
3400 North Charles Street, Baltimore, Maryland, 21218, USA

Gravitational-wave (GW) astronomy offers the potential to probe the wave-optics regime of gravitational lensing. Wave-optics (WO) effects are relevant at low frequencies, when the wavelength is comparable to the characteristic lensing time delay multiplied by the speed of light, and are thus often negligible for electromagnetic signals. Accurate predictions require computing the conditionally convergent diffraction integral, which involves highly oscillatory integrands and is numerically difficult. We develop and implement several methods to compute lensing predictions in the WO regime valid for general gravitational lenses. First, we derive approximations for high and low frequencies, obtaining explicit expressions for several analytic lens models. Next, we discuss two numerical methods suitable in the intermediate frequency range: (1) *regularized contour flow* yields accurate answers in a fraction of a second for a broad range of frequencies; and (2) *complex deformation* is slower, but requires no knowledge of solutions to the geometric lens equation. Both methods are independent and complement each other. We verify subpercent accuracy for several lens models, which should be sufficient for applications to GW astronomy in the near future. Apart from modeling lensed GWs, our method will also be applicable to the study of plasma lensing of radio waves and tests of gravity.

I. INTRODUCTION

Gravitational lensing, the deflection of waves by gravitational fields, has become an essential tool for exploring the Universe's structure and contents. The rich phenomenology of gravitational lensing [1] has enabled many applications, from inferring cosmological parameters to testing dark matter models. Progress on these fronts has relied exclusively on observations across the electromagnetic spectrum. However, recent advances in gravitational-wave (GW) astronomy [2,3] open up a new arena for gravitational lensing. In time, searches of lensed GWs [4,5] are likely to turn into conclusive detections and novel applications.

Differences between gravitational and electromagnetic radiation from astrophysical sources make GW lensing qualitatively distinct and complementary to electromagnetic observations. GWs emit coherently and at much lower frequencies. GWs detectable by LIGO-Virgo-KAGRA (LVK) have wavelengths that are more than 3 orders of magnitude longer than the lowest-frequency radio waves permitted by the Earth's ionosphere. This difference may allow the observation of wave-optics (WO) effects [6,7], which emerge when the wavelength is comparable to the time delay produced by the lens multiplied by the speed of light. WO effects are frequency dependent and their detection would allow an accurate determination of the lens properties [8–11]. Moreover, WO lensing of GWs could serve to identify stellar-scale microlenses [12–16] and test dark matter scenarios [6,17–23].

Unfortunately, accurately computing lensed waveforms in the WO regime is challenging. A closed-form analytical expression exists only for the simplest point-mass lens [24], and series expansions have been developed for more general lenses [25]. These solutions have been widely used to study WO lensing. However, even these simple expressions are costly to evaluate in practice, particularly at high frequencies. General predictions require conditionally

[*]giovanni.tambalo@aei.mpg.de
[†]miguel.zumalacarregui@aei.mpg.de
[‡]liangdai@berkeley.edu
[§]hcheung5@jhu.edu

convergent integrals of rapidly oscillating functions over the lens plane. Previous works used direct integration [6,26], Levin's algorithm method [27,28], sampling of the Fermat potential over contours [15,29] (related to our first method) or discretely [13,14,16], discrete fast-Fourier transform (FFT) convolution [30], and Picard-Lefschetz theory [31,32] (related to our second method). While these methods have been used to study complex lenses (e.g., Refs. [13–16]), they have been validated (e.g., cross-validated with independent calculations) only for simple examples.

Here we describe methods to obtain WO predictions and cross-validate them on several lens models. In Sec. II we present the diffraction integral. In Sec. III we present expansions valid in the low- and high-frequency limits before turning to general, numerical algorithms. In Sec. IV we solve the Fourier transform of the integral by adaptively sampling contours of equal time delay. Then, in Sec. V we analytically continue the integration variable to make the integral manifestly convergent. Finally, in Sec. VI we validate the accuracy of both methods and discuss their performance. We have explored the phenomenology of GW lensing separately [33]. Throughout this paper, we work in a unit system with $c = 1$.

II. WAVE-OPTICS REGIME OF GRAVITATIONAL LENSING

In this section we review the equations governing gravitational lensing in the WO regime. In order to focus on the mathematical problem we will not provide a detailed derivation of the quantities involved. Readers are referred to Refs. [8,33] for details. Our goal is to evaluate the diffraction integral, which we give in dimensionless form

$$F(w) = \frac{w}{2\pi i} \int d^2 x \, e^{iw\phi(x,y)}. \qquad (1)$$

See Ref. [34] for a derivation. The integration is over the lens plane, with the coordinates rescaled by a dimensionful scale ξ_0 (e.g., a characteristic scale of the lens), so x is dimensionless. The impact parameter y is rescaled by $\eta_0 \equiv D_S \xi_0 / D_L$, where D_S and D_L are the angular diameter distances to the lens and the source, respectively.

Here we introduced the *dimensionless frequency*

$$w \equiv 8\pi G M_{Lz} f, \qquad (2)$$

which is given in terms of a redshifted *effective lens mass*:

$$M_{Lz} \equiv \frac{\xi_0^2}{2G d_{\text{eff}}}. \qquad (3)$$

The factor $d_{\text{eff}} \equiv \frac{D_L D_{LS}}{(1+z_L) D_S}$ also depends on the angular diameter distance between the lens and the source D_{LS}. For a point lens, M_{Lz} coincides with the total mass of the

TABLE I. Summary of lens models used in this work. For reference, we have included $\rho(r)$, the density of a spherically symmetric matter distribution leading to the lensing potential ψ in each case.

Name	$\rho(r)$	$\psi(x)$	Parameters
Point lens	$\delta_D(r)$	$\log(x)$	
SIS	$\frac{1}{r^2}$	x	
gSIS	$\frac{1}{r^{(k+1)}}$	$\frac{x^{(2-k)}}{(2-k)}$	Slope k
CIS	$\frac{1}{r^2+r_c^2}$	$\sqrt{x_c^2 + x^2} + x_c \log\left(\frac{2x_c}{\sqrt{x_c^2+x^2}+x_c}\right)$	Core size x_c

lens (i.e., setting ξ_0 to be the Einstein radius), but this is not true for extended lenses.

The integral depends on the *Fermat potential*:

$$\phi(x,y) = \frac{1}{2}|x - y|^2 - \psi(x) - \phi_m(y). \qquad (4)$$

Here ψ is the lensing potential, which depends on the matter distribution projected onto the lens plane and whose derivative gives the deflection angle [Eq. (5) below]. We conventionally shift by $\phi_m(y)$, the global minimum value of the Fermat potential. From here on, we suppress $\phi_m(y)$ in our formulas and assume that it is added to make the minimum arrival time equal to zero. When necessary, we will reintroduce it.

We consider several lens models in this work, summarized in Table I. All of them are spherically symmetric, leading to an axisymmetric projected mass and lensing potential $\psi(x) = \psi(x)$ (here and in the following, $x \equiv |x|$). First, we consider the point lens, whose analytic solution will help us test the accuracy of different methods in Sec. VI. We additionally consider three extended lenses: the singular isothermal sphere (SIS) and two one-parameter extensions. SIS lenses follow from a matter profile $\rho \propto 1/r^2$ and are often employed to model lensing by galaxies. Our first extension, the generalized SIS (gSIS), has an arbitrary slope $\rho \propto 1/r^{1+k}$ ($0 < k < 2$) and can be used to model steeper or shallower lenses [34–36]. Its central density diverges, but the enclosed mass up to some radius remains finite if $k < 2$. Our second extension, the cored isothermal sphere (CIS), has a central core of physical radius $r_c = x_c \xi_0$ [37,38]. Therefore, the matter density $\rho \propto 1/(r^2 + r_c^2)$ is finite at the center. Details about these lenses and their phenomenology are provided separately [33].

Figure 1 shows the amplification factor for an SIS lens with impact parameter $y = 0.3$. The full WO solution is obtained by regularized contour flow (discussed in Sec. IV) matched to an analytic expansion at high frequencies. The remaining curves correspond to the expansions presented in Sec. III, each with a limited range of validity: geometric optics (GO) and its next-order refinement (bGO) (Sec. III A) are good descriptions at high frequency, while the series expansion (Sec. III B) is a good approximation only for
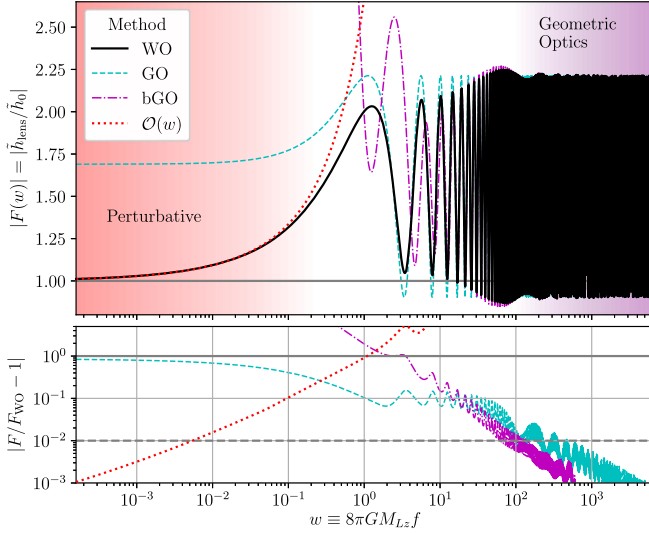
FIG. 1. Amplification factor for an SIS lens ($y = 0.3$). Top: the full WO solution (solid) is compared to different approximations: low-w series expansion (dotted), geometric optics (dashed), and beyond geometric optics (dash-dotted). The regions where systematic expansions are good descriptions are shaded. Bottom: relative deviation with respect to the WO solution.

$w \ll 1$. GO remains bounded at all frequencies, while bGO and the series expansion diverge at low and high frequencies, respectively.

III. ANALYTIC EXPANSIONS

We now present analytic expansions valid in the high- and low-frequency limits in Secs. III A and III B, respectively.

A. Geometric optics and beyond

In the high-frequency limit, following the same arguments leading to the stationary-phase approximation for path integrals, only the neighborhoods of extrema of the Fermat potential (4) contribute to the amplification factor (1). Each extremum is associated with an image J, located at a position x_J in the image plane where the lens equation

$$\nabla_x \phi(x_J, y) = x_J - y - \alpha(x_J) = 0 \tag{5}$$

is satisfied [here $\alpha(x_J) \equiv \nabla_x \psi(x_J)$ is the deflection angle and ∇_x is the gradient computed with respect to x]. The *geometric optics* regime emerges from a quadratic expansion of the Fermat potential around each image so that the diffraction integral can be performed analytically.

The GO amplification factor (1) receives contributions from each image J,

$$F(w) = \sum_J |\mu_J|^{1/2} e^{iw\phi_J} e^{-i\pi n_J}, \tag{6}$$

where the *magnification*

$$\mu^{-1} \equiv \det(\phi_{,ij}) = \left(1 - \frac{\alpha(x)}{x}\right)\left(1 - \frac{d\alpha(x)}{dx}\right) \tag{7}$$

is evaluated at the image position x_J (the second equality above applies to the specific case of axially symmetric lenses). In the above expressions, ϕ_J is the Fermat potential of the Jth image, $\phi_{,ij} \equiv \partial_i \partial_j \phi$ is its Hessian matrix, and $\alpha(x) \equiv |\alpha(x)|$. As we are working in the two-dimensional lens plane, $i, j, \ldots \in \{1, 2\}$, corresponding to the x_1 and x_2 coordinates (the Cartesian components of x). The *Morse phase* [8,34,39] depends on the type of image as

$$n_J = \begin{cases} 0 & \text{if } \det(\phi_{,ij}), \text{tr}(\phi_{,ij}) > 0 & \text{(minima)}, \\ \frac{1}{2} & \text{if } \det(\phi_{,ij}) < 0 & \text{(saddle)}, \\ 1 & \text{if } \det(\phi_{,ij}) > 0, \text{tr}(\phi_{,ij}) < 0 & \text{(maxima)}. \end{cases} \tag{8}$$

Minima, saddle points, and maxima of the time delay function are also known as type I, II, and III images, respectively [40].

1. Beyond geometric optics

bGO corrections can be obtained as a series expansion in $1/w$. We now review the leading bGO correction, following Ref. [26] and focusing on axially symmetric lenses (see also Ref. [41]). First of all, we expand the lensing potential ϕ around each image x_J up to quartic order in $\tilde{x}^i \equiv x^i - x_J^i$:

$$\phi(x, y) = \phi_J + \frac{1}{2}(\phi_J)_{,ij}\tilde{x}^i\tilde{x}^j + \frac{1}{3!}(\phi_J)_{,ijk}\tilde{x}^i\tilde{x}^j\tilde{x}^k$$
$$+ \frac{1}{4!}(\phi_J)_{,ijkl}\tilde{x}^i\tilde{x}^j\tilde{x}^k\tilde{x}^l + \mathcal{O}(\tilde{x}^5). \tag{9}$$

For a symmetric lens, the quadratic term in $\tilde{x}^i$ is diagonal and can be written as (here y is taken to be along the x_1 direction so that $x^i_J = x_J \delta^i_1$)

$$(\phi_J)_{,ij}\tilde{x}^i\tilde{x}^j = (1 - \psi_J'')\tilde{x}_1^2 + \left(1 - \frac{\psi_J'}{x_J}\right)\tilde{x}_2^2$$
$$= 2a_J\tilde{x}_1^2 + 2b_J\tilde{x}_2^2, \tag{10}$$

where primes denote radial derivatives and we defined $a_J \equiv (1 - \psi_J'')/2$ and $b_J \equiv (1 - \psi_J'/x_J)/2$. At this point, in the diffraction integral (1) we shift and rescale x^i to $z^i \equiv \sqrt{w}\tilde{x}^i$. In terms of z^i, the quadratic term at the exponent is w independent. The cubic and quartic terms of Eq. (9), multiplied by w, scale instead as $\mathcal{O}(w^{-1/2})$ and $\mathcal{O}(w^{-1})$, respectively. For large w, we can then Taylor expand the exponential and keep terms up to $\mathcal{O}(w^{-1})$.

At order $\mathcal{O}(w^0)$ we recover the GO result (from the quadratic part). The term of order $\mathcal{O}(w^{-1/2})$ vanishes since it leads to an odd integrand. The first correction comes

instead at order $\mathcal{O}(w^{-1})$, where we have two distinct contributions: one from squaring the term $(\phi_J)_{,ijk}\tilde{x}^i\tilde{x}^j\tilde{x}^k$ and another from $(\phi_J)_{,ijkl}\tilde{x}^i\tilde{x}^j\tilde{x}^k\tilde{x}^l$. Terms with higher powers of $\tilde{x}$ contribute at order $\mathcal{O}(w^{-3/2})$ or higher, and can thus be neglected at sufficiently large frequencies.

After performing these two integrals, one is left with the following simple result:

$$F(w) = \sum_J |\mu_J|^{1/2}\left(1 + i\frac{\Delta_J}{w}\right)e^{iw\phi_J - i\pi n_J} + \mathcal{O}(1/w^2), \quad (11)$$

where the real number Δ_J characterizes the bGO correction and is given by

$$\Delta_J \equiv \frac{1}{16}\left[\frac{\psi_J^{(4)}}{2a_J^2} + \frac{5}{12a_J^3}(\psi_J^{(3)})^2 + \frac{\psi_J^{(3)}}{a_J^2 x_J} + \frac{a_J - b_J}{a_J b_J x_J^2}\right]. \quad (12)$$

Here $\psi^{(n)} \equiv \frac{d^n}{dx^n}\psi$.

Equation (11) shows that the leading-order GO result is a good approximation provided that $\Delta_J/w \ll 1$ for all images.[1] Note also that nonanalytic features in the Fermat potential (e.g., cusps) produce other $\mathcal{O}(w^{-1})$ contributions without a corresponding GO image [26]. We now address the contribution of nonanalytic features in specific cases.

2. Contribution from the cusp

The leading terms in the GO expansion, Eq. (6), arise from the stationary points of the Fermat potential and capture the high-w contributions to the amplification factor. Nonetheless, other locations in the lens plane can induce corrections at subleading order in the $\sim 1/w^n$ expansion and might be comparable to the bGO terms. In particular, they can arise from singular points of the lens equation (cusps in the lensing potential). See Ref. [26] for a similar discussion on cusp contributions to $F(w)$.

In this subsection we discuss these contributions for the lens models featuring a central cusp (gSIS and SIS lenses; Table I).[2] In particular, we focus on the strong-lensing regime, where y can be taken as a small number.

Let us consider the gSIS lens in the limit of large w. For this lens, we distinguish two behaviors depending on the value of the slope k. For $0 < k < 1$ (broad profiles) the lens equation is smooth at the lens' center and a central image forms in the strong-lensing regime. In other terms, the deflection angle α is bounded as the ray approaches the

center of the lens. In the complementary interval $1 \leq k < 2$ (narrow profiles) the lens equation is singular at the center and no image forms. In both cases we isolate the contribution to $F(w)$ from the center by truncating the integration range from $x \in (0, R_c)$, for some radius R_c small enough for the GO images to not be enclosed. The range $x > R_c$, at high w, is then dominated by the GO expansion around the minimum and/or saddle (depending on y). In the lower integration interval, we have instead

$$F_c(w) = \frac{w}{2\pi i}\int_0^{R_c} dx\, x \int_0^\pi d\theta e^{iw\phi(x,y)}$$
$$= -iwe^{iw\phi_c}\int_0^{R_c} dx\, x J_0(wyx)e^{iw(\frac{x^2}{2} - \psi(x))}, \quad (13)$$

where $\phi_c \equiv y^2/2 - \phi_m$ is the time delay associated with the lens center (here we reintroduced the minimum time delay ϕ_m) and $J_\nu(z)$ is the Bessel function of the first kind (obtained after performing the angular integral). The integrand, in the limit $w \gg 1$, peaks around $x = 0$ once we rotate the integration line into the complex plane. To see this, first notice that $J_0(wyx)e^{iwx^2/2} \simeq 1$ for small x (we will better motivate why x can be taken small *a posteriori*). By writing $xe^{-iw\psi(x)} = e^{\log x - iw\psi(x)} \equiv e^\Omega$, we can locate the peak as the stationary point x_s of Ω:

$$\frac{d}{dx}\Omega = \frac{1}{x_s} - iwx_s^{1/A-1} = 0. \quad (14)$$

Here we defined $A \equiv 1/(2 - k)$, which is a positive quantity. Equation (14) is solved for $x_s = (iw)^{-A}$. Notice that x_s becomes smaller for larger w, making our approximation adequate in this limit [in particular, the Gaussian part at the exponent can be neglected since $x_s^2 \ll \psi(x_s)$].

Therefore, $F_c(w)$ for $w \gg 1$ can be obtained using a saddle-point approximation around x_s. However, we prefer to take a slightly different approach that yields very similar results: we evaluate $J_0(wyx)e^{iwx^2/2}$ in Eq. (13) at the peak x_s, while performing the exact integration for e^Ω. Since the integral is highly localized for $w \gg 1$, the calculation can be simplified by taking $R_c \to \infty$, making exponentially small errors. We obtain

$$F_c(w) \simeq -iwe^{iw\phi_c}J_0(wyx_s)e^{iwx_s^2/2}\int_0^\infty dx\, xe^{-iw\psi(x)}$$
$$= -e^{iw\phi_c}(iwA)^{1-2A}\Gamma(2A)J_0(wyx_s)e^{iwx_s^2/2}. \quad (15)$$

This formula is valid when the limits $w \gg 1$ and $wyx_s \ll 1$ are satisfied (therefore, for small enough y).[3] The full $F(w)$ is then given by the sum of Eq. (15) and the usual GO

---

[1]Another GO convergence criterion is that $w(\phi_I - \phi_J) \gg 1$, $\forall I \neq J$. This can be understood from the contours framework (IV) as the images being resolvable at finite frequency. Note that this criterion is, in general, independent from bGO terms being negligible, $\Delta/w \ll 1$.

[2]The center is smooth for the CIS lens, so no new contribution arises compared with bGO. The point lens is singular at the center, but the new contribution is highly suppressed in w (see Ref. [26] for a discussion). Thus, the gSIS is the only relevant case among the lenses we consider.

[3]Contribution from cusps were computed in Ref. [26] for SIS and gSIS lenses. For the SIS, Eq. (15) matches Eq. (21) of Ref. [26] for small y. For the generic gSIS instead, Ref. [26] implicitly assumed large y, so that our formulas cannot be directly compared.

expansion for the other images. In the following, we will refer to this expansion as *resummed* GO (rGO). We can better understand the behavior of $F_c(w)$ by first looking at the SIS case $k = 1$. Here, neglecting again the Gaussian and the Bessel function, we have $F_c(w) \simeq i/we^{iw\phi_c}$. This can be interpreted as an additional bGO contribution from the cusp $x = x_c = 0$, with time delay ϕ_c and with a vanishing GO term (i.e., not accompanied by an image). More generally, for narrow (broad) profiles, $F_c(w)$ decays faster (slower) than $1/w$.

For broad profiles, there is a caveat in the previous derivation at very large w: the Gaussian part can start contributing significantly to the integral, thus leading to the usual GO expansion for the central image. Therefore, for $0 < k < 1$, F_c in Eq. (15) is a better approximation than bGO for the central image only in the range $1 \lesssim w \lesssim \Delta_c$, while for $\Delta_c/w \ll 1$ bGO performs better [here Δ_c is the bGO coefficient of the central image, Eq. (12)]. This issue does not arise for $k > 1$, since here there is no central image.

From the discussion above we conclude that WO effects from the cusp are relevant even when no central image forms. As we study in Ref. [33], this has interesting implications for parameter estimations with GWs.

B. Low-frequency expansion

We are now interested in understanding the behavior of the amplification factor in the limit of small w. In this limit, GO fails and one has to resort to other methods to obtain good approximations.

For small w, $F(w)$ approaches 1 since the wavelength becomes much larger than the lens' characteristic scale, and the wave is unperturbed by the lens. Here we would like to show that corrections to $F(w) \sim 1$ in this limit correspond to an expansion in powers of the lensing potential $\psi(x)$. A physical motivation can be given as follows. If the wavelength is much larger than the typical scale of the lens (i.e., the Einstein radius), then the impact parameter's value cannot be precisely resolved. This implies that the impact parameter should be irrelevant (at least at leading order) in this low-frequency limit. Thus, we could imagine performing the calculation for $F(w)$ with $y \gg 1$ (i.e., the impact parameter is much larger than the scale of the lens, set by ξ_0) but still much smaller than the wavelength $\propto 1/w$. In this case one can expand the diffraction integral in powers of the lensing potential (see Ref. [42] for the conditions for the applicability of this approximation).

We can also see explicitly that this procedure gives a sensible series expansion in w: higher powers in $\psi(x)$ lead to subleading terms in w. For simplicity, we show this for axisymmetric lenses.

First, we perform a rotation of the integration contour to make the integrals manifestly convergent. Similarly to Eq. (13), the amplification factor can be written as follows:

$$F(w) = -iwe^{iwy^2/2} \int_0^\infty dx x J_0(wyx) e^{iw(x^2/2-\psi(x))}$$

$$= e^{iwy^2/2} \int_0^\infty dz z J_0(e^{i\pi/4}\sqrt{w}yz) e^{-z^2/2-iw\psi(x(z))}, \quad (16)$$

where in the second line we rescaled the radial variable and rotated the integration contour by 45 degrees in the complex plane, $x = e^{i\pi/4}z/\sqrt{w}$.[4] Note that the Gaussian part dictates the leading behavior at infinity of the integrand, since the Bessel function only grows exponentially and we assume for convergence that $|\psi|$ grows more slowly than the argument of the Gaussian [$\lim_{x\to\infty} |\psi|/x^2 = 0$; see Eq. (19) below]. Thus, convergence is now manifest. However, this choice for the integration contours is not optimal: the Bessel function and the lensing potential can make the integrand exponentially large at intermediate values of z, for large w. On the other hand, for small w, Eq. (16) is easy to evaluate, giving us a tool to explore $F(w)$ in the WO regime. We will discuss how to obtain the optimal integration contour for more general lenses in Sec. V.

After this first step, we can expand the integrand in powers of $\psi(x(z))$. Equation (16), expanded in $\psi(x(z))$ up to quadratic order, has the form

$$F(w) \simeq 1 - e^{iwy^2/2} \int_0^\infty dz z e^{-z^2/2} J_0(e^{i\pi/4}\sqrt{w}yz)$$

$$\times \left[iw\psi\left(\frac{e^{i\pi/4}z}{\sqrt{w}}\right) + \frac{w^2}{2}\psi\left(\frac{e^{i\pi/4}z}{\sqrt{w}}\right)^2 \right]. \quad (17)$$

Obtaining higher terms in this expansion is also trivial. If ψ is well behaved for large z, then the integrals in Eq. (17) are localized around $z = 1$ and can be estimated through a steepest-descent calculation.[5] See Ref. [36] for a similar expansion, but in the weak-lensing regime.

Let us first consider $y = 0$ for simplicity. With the $z = 1$ approximation, we obtain

$$F \simeq 1 - iw\psi\left(\frac{e^{i\pi/4}}{\sqrt{w}}\right) - \frac{w^2}{2}\psi\left(\frac{e^{i\pi/4}}{\sqrt{w}}\right)^2. \quad (18)$$

This is a series in powers of $w\psi(e^{i\pi/4}/\sqrt{w})$; higher powers in the expansion are suppressed for small w provided that

$$\lim_{w\to 0} w\psi(e^{i\pi/4}/\sqrt{w}) = 0. \quad (19)$$

---

[4] Here we implicitly assumed $\psi(x)$ to be analytic in the region $0 \leq \arg x < \pi/2$ of the complex-x plane. For the lenses we consider in Table I this is the case and it is possible to perform the 45-degree rotation in the complex plane without hitting singularities. For more general situations, Eq. (17) needs to be modified to include the contribution of singularities.

[5] Note that this is just an approximation we can use to estimate the integrals, and does not reduce to the exact answer in any limit. This approximation is often not required for specific lens models, as one can just evaluate the integrals exactly.

This condition is physically sensible since it is equivalent to the requirement for $\psi(x)$ to grow less than the quadratic part of the lensing potential at infinity (in this particular direction of the complex plane). Equivalently, in terms of the density profile ρ, the requirement translates to ρ decaying faster than $\propto 1/r$ at infinity. All of the analytic lens models we consider in this work satisfy this requirement, and hence this expansion is applicable in our cases.

The conclusion that Eq. (17) is a good expansion for small w is not spoiled in the case of $y \neq 0$. To see this, we first notice that y enters only the combination wy^2 in Eq. (17). Hence, if wy^2 is smaller than 1, we can expand the Bessel function in a series around zero (the integral is localized around $z = 1$ and the argument of J_0 remains small). In the limit $w \ll 1$ this is possible, with the mild requirement of $y \ll 1/\sqrt{w}$. Additionally, we can also notice that y will not enter at first order in the w expansion of $F(w)$. Indeed, the series expansion $J_0(e^{i\pi/4}\sqrt{w}yz) \simeq 1 - \frac{i}{4}wy^2z^2 + \mathcal{O}(w^2y^4z^4)$ shows that effects due to y are suppressed by additional powers of w.

1. Leading corrections for symmetric lenses

After these general results, we can focus on the low-w behavior for the specific lenses shown in Table I. For the simplest cases, we can directly integrate Eq. (17) without assuming small y.

Point lens: In this case, $\psi(x) = \log x$ and the integral in Eq. (1) has a closed-form solution [8]:

$$F(w) = e^{\frac{\pi}{4}w + i\frac{w}{2}(\log(\frac{w}{2}) - 2\phi_m)}\Gamma\left(1 - i\frac{w}{2}\right){}_1F_1\left(\frac{iw}{2}, 1, iw\frac{y^2}{2}\right),$$
(20)

where $\phi_m = (x_m - y)^2/2 - \log(x_m)$ is the minimum of the Fermat potential, evaluated at $x_m = (y + \sqrt{y^2 + 4})/2$. Moreover, ${}_1F_1(a, b, z)$ is the confluent hypergeometric function. We can nonetheless employ the low-frequency expansion and then compare with the formula above, expanded in the same limit. Equation (17) (neglecting $w^2\psi^2$ terms) gives

$$F^{\mathrm{pl}} \simeq 1 + \frac{w}{2}[\pi - i(2\log y - \mathrm{Ei}(iwy^2/2))] + \mathcal{O}(w^2),$$
(21)

where $\mathrm{Ei}(z)$ is the exponential integral. We checked that indeed Eq. (20) expanded for small w, but fixed wy^2, yields Eq. (21). It is also useful to further expand Eq. (21) for small wy^2:

$$F^{\mathrm{pl}} \simeq 1 + \frac{w}{4}\left(\pi + 2i\gamma_{\mathrm{E}} + 2i\log\frac{w}{2}\right) + \mathcal{O}(w^2y^2),$$
(22)

where γ_{E} is Euler's constant.

Let us briefly digress and comment about the analytic properties of Eq. (22) as a function of w. We can first note that the diffraction integral, Eq. (1), is analytic for $\mathrm{Im}\, w > 0$, while possible nonanalyticities can appear on the real axis and in the lower half of the complex plane. The analyticity property for $\mathrm{Im}\, w > 0$ is a consequence of causality: while the lensed signal can have a distorted waveform due to diffraction, no signal can travel beyond the light cone (see Refs. [43,44] for a related discussion). The above properties can be checked for the point lens, using its closed-form solution (20). The latter formula is indeed analytic for $\mathrm{Im}\, w > 0$, and has poles due to the gamma function for $\mathrm{Im}\, w < 0$ and a branch cut due to the $\log w$ for negative w. Notice that by construction $F(w)$ satisfies a reality condition, $F^*(w) = F(-w)$. The non-analyticity of $F(w)$ and the reality condition imply that $F(w)$ must be a complex number for real w; otherwise, it would be either real or imaginary. By direct inspection, Eq. (22) is consistent with these properties. In particular, a branch cut appears due to $\log w$. Similar considerations apply to the lens models of Table I.

SIS lens: Here, $\psi(x) = x$ and keeping up to the ψ^2 term in Eq. (17) we obtain (again keeping wy^2 fixed)

$$F^{\mathrm{SIS}} \simeq 1 - \frac{e^{i\pi/4}}{4}\sqrt{2\pi w}e^{iwy^2/4}\left[2i\left(1 - \frac{iwy^2}{2}\right)J_0(wy^2/4)\right. \\ \left. - iwy^2J_1(wy^2/4)\right] - \frac{w}{2}(2i + wy^2) + \mathcal{O}(w^{3/2}).$$
(23)

After expanding the expression above for small y, we obtain

$$F^{\mathrm{SIS}} \simeq 1 - (-1)^{3/4}\sqrt{\frac{\pi w}{2}} - iw + \mathcal{O}(w^{3/2}).$$
(24)

Interestingly, in this case the leading behavior in w differs from that of the point lens. The dependence on $\sqrt{w}$ can be understood from Eq. (17). If we call $s \equiv \sqrt{w}y$ and use $\psi(x) = x$, we see that the only dependence on w is through $\sqrt{w}$. Together with the fact that s will not appear at leading order, we obtain the correct dependence of F. The slope as a function of $\sqrt{w}$ is related to the steepness of $\psi(x)$ far from the center of the lens. This can be seen by considering a generalized SIS lens, with a generic slope.

Generalized SIS lens: The gSIS lens, as already discussed, is described by the lensing potential $\psi(x) = x^{2-k}/(2 - k)$, where the slope is parametrized by $0 < k < 2$. The case $k = 1$ reduces to the SIS.

The first-order expansion in w leads to

$$F^{\mathrm{gSIS}} \simeq 1 + (-w/2)^{k/2}\Gamma(1/2A)e^{iw\frac{y^2}{2}}L_{1/2A}(iwy^2/2) \\ + \mathcal{O}(w),$$
(25)

where $\Gamma(z)$ is the gamma function, $L_\alpha(z)$ are the Laguerre polynomials, and we again introduced $A = 1/(2 - k)$. Expanding for small y leads simply to

$$F^{\text{gSIS}} \simeq 1 + (-w/2)^{k/2}\Gamma(1/2A) + \mathcal{O}(w). \quad (26)$$

This expression agrees with what was found in Ref. [36]. Notice that the leading term in w depends on the slope k: steep lenses (k close to zero) have a weaker dependence on w.

CIS lens: This lens represents an SIS lens with a central core of size x_c. Its lensing potential is given in Table I. As we have argued, in the limit of low w we are mainly sensitive to the profile of the lens far away from the center. Thus, we expect to have a weak dependence on x_c in this limit. We do not know a closed expression for the integrals of $\psi(x)$ in Eq. (17). However, we can approximate them by noticing that since the integral is peaked around $z \sim 1$ and we are interested in $w \ll 1$, we can simply expand $\psi(e^{i\pi/4}z/\sqrt{w})$ for large arguments. Interestingly, for large x we have $\psi(x) \simeq x - x_c \log \frac{x}{2x_c} + \mathcal{O}(1/x)$. In other words, the lens looks like an SIS plus a central point lens with negative mass. Notice that to correctly capture the dependence on x_c we need to include the second-order correction from Eq. (17). By doing so, we obtain

$$F^{\text{CIS}} \simeq 1 + (F^{\text{SIS}} - 1) - x_c(F^{\text{pl}} - 1) \\ - iwe^{-iwy^2/2}[x_c \log (2x_c) + 1 - iwy^2/2]. \quad (27)$$

More explicitly, by further expanding for small y we have

$$F^{\text{CIS}} \simeq 1 - \left[(-1)^{3/4}\sqrt{\frac{\pi w}{2}} + \frac{wx_c}{4}\left(2i\gamma_{\text{E}}\right.\right. \\ \left.\left. + \pi + 2i \log \frac{w}{2} + 4i \log(2x_c) + \frac{4i}{x_c}\right)\right]. \quad (28)$$

This result shows that the leading behavior in w is due to the SIS part, while the presence of the core is only visible at subleading order. From Eq. (28) we notice that increasing x_c leads to a *smaller* $|F(w)|$. This is consistent with our numerical results. Later, we will test the accuracy of this approximation against the full WO result (Sec. VI B, Fig. 9).

Throughout this discussion we have suppressed the minimum time delay ϕ_m [see discussion below Eq. (4)]. To reintroduce this parameter, all of the expanded expressions for $F(w)$ in this section should be multiplied by the phase $e^{-iw\phi_m}$.

2. gSIS series expansion

The amplitude factor for simple lens models can be written in a useful series representation by expanding the integrand in powers of the lensing potential $\psi(x)$. In particular, we will be able to obtain such representations for the SIS and gSIS lens models (see Table I). This provides

an additional independent test of our numerical methods, which will be very valuable to validate our results. We first consider a generic axially symmetric $\psi(x)$ and later specialize to particular functional forms. To proceed, we start from Eq. (1) and perform the angular integral, which yields the usual Bessel function $J_0(wyx)$ [already encountered in Eq. (17)]. After this, we expand $e^{-iw\psi(x)}$ in powers of $\psi(x)$ and notice that when $\psi(x)$ is a power-law function of x, each integral in the series expansion can be performed analytically. In the case of a gSIS lens we have

$$F(w) = -iwe^{\frac{i}{2}wy^2} \sum_{n=0}^{\infty} \frac{1}{n!}\left(\frac{-iw}{2-k}\right)^n \\ \times \int_0^{+\infty} dx\, x^{1+n(2-k)}J_0(wxy)e^{iwx^2/2} \\ = \sum_{n=0}^{\infty} \frac{\Gamma(\frac{n}{2A}+1)}{n!}[2^{\frac{1}{2A}}A(-iw)^{k/2}]^n L_{\frac{n}{2A}}(iwy^2/2), \quad (29)$$

where once again $A = 1/(2 - k)$. Notice that for low w this expansion reduces to our approximation obtained in Eq. (25). Moreover, in the particular case of $k = 1$ (SIS) we reobtain the series representation first derived in Ref. [25]:

$$F(w) = e^{\frac{i}{2}wy^2} \sum_{n=0}^{\infty} \frac{\Gamma(1+\frac{n}{2})}{n!} \\ \times (2we^{i\frac{3\pi}{2}})^{n/2}\,_1F_1\left(1+\frac{n}{2}, 1, -\frac{i}{2}wy^2\right). \quad (30)$$

In order to recover the oscillatory features of $F(w)$ accurately for large enough w, the series in Eqs. (29) and (30) need to be truncated at relatively high values of n. In our comparisons this truncation is made after reaching a 10^{-15} precision. As an example, for $w = 200$ and $y = 0.3$ this is obtained at around $n = 740$. For lower w at fixed y, convergence is reached at lower n. As a result, the features due to the GO, bGO, and rGO terms are not manifest from this series expansion.

The series (29) is impractical for most applications, since the evaluation of the Laguerre polynomials is slow. Moreover, for an imaginary argument they grow exponentially in n. Therefore, many terms in the series are required to reach convergence, even at moderate w. Thus, as we will see, these results are outcompeted by numerical implementations of the diffraction integral in practical applications. Additionally, this series expansion is difficult to generalize to other lens models such as the CIS lens, since in that case we do not have a closed-form solution for the integrals.

IV. REGULARIZED CONTOUR FLOW

We now turn to general methods to numerically solve Eq. (1). This section presents the regularized contour flow, a calculation performed by Fourier transforming the integral in Eq. (1) and evaluating the resulting time-domain integral on contours of equal time delay. Each set of

contours is then flowed adaptively to a different value of the time delay until "hitting" a critical point, when the contour ends (several contours end at saddle points). The total integral is transformed back to frequency space by means of an FFT, after splitting the result into regular, smooth, and singular contributions, associated with GO results. We follow Ref. [29] (see also Ref. [45]) but use a different regularization for the saddle points. The steps in the method are described in Fig. 2, and the precision parameters and their default values are listed in Table II.

A. Adaptive sampling in the time domain

We first compute the amplification factor in time-delay space. Fourier transforming the integrand in Eq. (1) yields

$$\tilde{I}(\tau) = \frac{1}{2\pi} \int d^2x \int_{-\infty}^{+\infty} dw \, e^{iw(\phi(\boldsymbol{x},\boldsymbol{y})-\tau)}$$
$$= \int d^2x \, \delta_D(\phi(\boldsymbol{x},\boldsymbol{y}) - \tau), \tag{31}$$

where $\delta_D(x)$ is the Dirac delta function. This expression is the primitive of the Green function: the time-domain lensed waveform is given by $h(t) = \int d\tau d\tilde{I}(\tau - t)/d\tau h_0(\tau)$. One can compute the function $\tilde{I}(\tau)$ by binning in time delays, cf. Refs. [13,14]. Instead, in this approach we reduce the two-dimensional (2D) integral to a one-dimensional (1D) integral over the contours where the argument of the Dirac delta is zero:
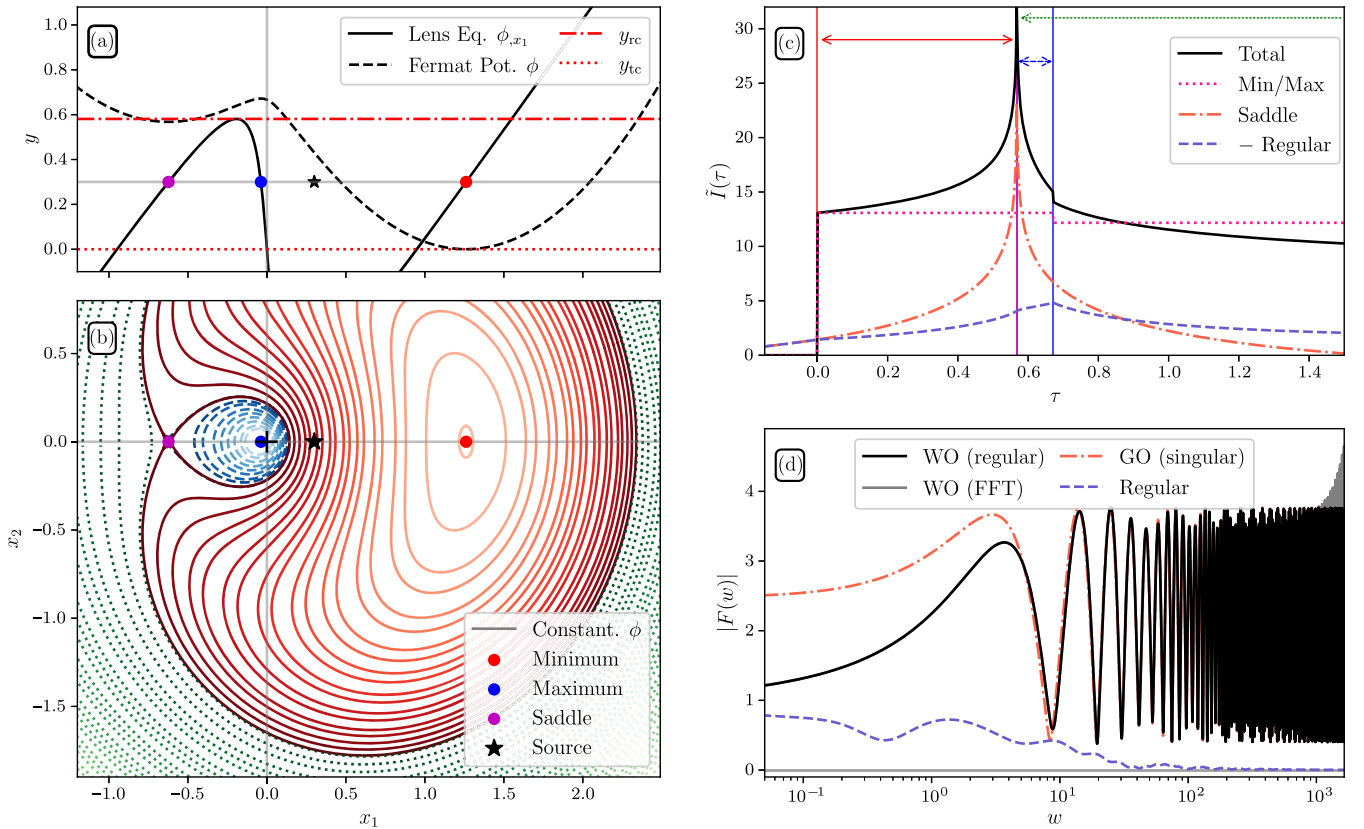

FIG. 2. WO lensing via contour flow with regularization. The lens is a cored isothermal sphere (see Sec. II and Table I) with a core size $x_c = 0.05$, impact parameter $y = 0.3$, and zero external convergence and shear. Panel (a): images are found across the lens-center-source axis by solving the lens equation. Images are located at stationary points of the Fermat potential ϕ (dashed line). Caustics are shown in red. Panel (b): the time-domain integral $\tilde{I}(\tau)$ [Eq. (32)] is computed across equal-time contours in the lens plane. The contours start at infinity (dotted) and the maximum (dashed) and minimum of ϕ (solid), and are evolved until they approach the saddle point (purple dot). Panel (c): $\tilde{I}(\tau)$ is computed by summing the contributions from all contours. Horizontal arrows show the extent of each contour from panel (b), ending at $\tau \to \phi_J$ (vertical lines). The singular contributions from maxima/minima (dotted) and the saddle point (dash-dotted) are removed, leaving the regular part $\tilde{I}_{\text{reg}}(\tau)$ (dashed). Panel (d): WO amplification factor. The total $F(w)$ [solid, Eq. (37)] is the sum of a regular piece (dashed), obtained by Fourier transforming $\tilde{I}_{\text{reg}}(\tau)$, and GO contributions for all of the images (dash-dotted). Fourier transforming the total $\tilde{I}(\tau)$ without splitting regular and singular contributions introduces numerical error at high frequencies (solid gray).

TABLE II. Summary of the precision parameters used for the contour method. Here $d_{l,m}$ is the distance between the l,mth node points and R_l is the local curvature radius of the contour evaluated at the lth node.

Parameter	Value	Description
Contour initialization:		
r_out	30	Outer contour radius
r_in	10^{-3}	Contour radius at min/max
nodes_ini	500	Initial nodes in contour
Contour adaptive flow, Eq. (34):		
dtau_0	10^{-4}	Initial $\Delta\tau$
η	0.1	Adaptive step size, Eq. (35)
η'	1.5	
dtau_min	10^{-4}	Minimum variation
dtau_max	0.1	Maximum variation
max_steps	10^4	Maximum number of steps
Contour node refinement:		
$\delta_{\max}$	0.02	Insert new node if $d_{k-1,k} > \delta_{\max} R_k$
$\delta_{\min}$	0.005	Remove k node if $d_{k-1,k+1} < \delta_{\min} R_k$
nodes_min	10	Minimum nodes in contour
FFT parameters:		
$\tau_{\max}$	500	Maximum sampled τ
N_{FFT}	2^{17}	FFT points
tau_min_extend	-0.1	Added to minimum sampled τ
Regularization:		
window_width	0.2	Window function width (relative)
T	30	Saddle point width, Eq. (43)

$$\tilde{I}(\tau) = \sum_k \oint_{\gamma_k} \frac{ds}{|\boldsymbol{\nabla}_x \phi(\boldsymbol{x}(\tau,s),\boldsymbol{y})|}, \qquad (32)$$

where s is the arc-length distance that parametrizes the kth contour γ_k of constant τ. [It is possible to reparametrize the contour so the integrand in Eq. (32) reduces to $\int du$, cf. Eq. (9) of Ref. [29].] The sum is over all contours contributing to a given τ (see below).

Contours of constant Fermat potential are orthogonal to the gradient of ϕ, and hence are given by

$$\frac{\partial \boldsymbol{x}(\tau,s)}{\partial s} \cdot \boldsymbol{\nabla}_x \phi(\boldsymbol{x},\boldsymbol{y}) = 0. \qquad (33)$$

To sample $\tilde{I}(\tau)$, we flow the contours as

$$\boldsymbol{x}(\tau + \Delta\tau, s) \simeq \boldsymbol{x}(\tau,s) + \Delta\tau \frac{\boldsymbol{\nabla}_x \phi}{|\boldsymbol{\nabla}_x \phi|^2}, \qquad (34)$$

i.e., each point is displaced (linearly) in the direction of the Fermat potential's gradient, with $\Delta\tau$ positive/negative if τ is increasing/decreasing. The integral $\tilde{I}(\tau)$ is sampled adaptively on each family of contours. We choose the step $\Delta\tau$ depending on the rate of variation $\tilde{I}$, according to the following prescription:

$$\Delta\tau_{i+1} = \min\left(\eta \frac{|d\tilde{I}/d\tau|}{|d^2\tilde{I}/d\tau^2|}, \eta'\Delta\tau_i, \right). \qquad (35)$$

Here η, η' are precision parameters and $d\tilde{I}/d\tau$, $d^2\tilde{I}/d\tau^2$ are computed numerically from the previous iterations. The variation $\Delta\tau$ is kept within minimum and maximum values. The algorithm stops if a prescribed number of iterations is reached.

At each step τ_i we refine the contour so the distance between its nodes is small compared to the local curvature radius of the contour (see Table II). Contours are flowed until reaching a critical point, where they either shrink to a point (maxima, minima, and cusps) or become nondifferentiable (saddle points). Therefore, we first find the critical points $\boldsymbol{x}_J$ such that $\boldsymbol{\nabla}_x \phi(\boldsymbol{x}_J, \boldsymbol{y}) = 0$ (i.e., GO images) [Eq. (5)]. Since we work with symmetric lenses we search only along the lens-source direction $x_1 \equiv \boldsymbol{x} \cdot \boldsymbol{y}/y$ (Figs. 2(a) and 2(b)).

For a given value of τ there can be zero, one, or multiple contours depending on the lens configuration. The total number of contours changes when τ crosses the values of the time delay ϕ_J associated with critical points and the integrand in Eq. (34) becomes singular. Hence, critical points are associated with singularities and discontinuities of $\tilde{I}(\tau)$. Contours do also end at nonregular points of the lensing potential, which are not associated with GO images.[6]

In the weak-lensing regime there is a single type I image at the minimum of ϕ; the contours then flow between the minimum and infinity, where they approach circles/ellipses centered around the source. Strong lenses produce multiple contours in certain ranges of τ. For the SIS, gSIS, and CIS in the strong-lensing regime there are three regions to consider: (1) from infinity down to the saddle point, (2) from the minimum up to the saddle point, and (3) from the maximum down to the saddle point. Contours that begin near the minimum/maximum are initiated with a small radius around the critical points. The contour that asymptotes to infinity is initiated at a large radius around the source (see Table II). These regions and their contributions to $\tilde{I}(\tau)$ are shown in Figs. 2(b) and 2(c).

B. Time-domain regularization and GO counterterms

The frequency-domain amplification factor can be computed from Eq. (31) via an inverse Fourier transform. We perform this operation via an FFT, for which we interpolate $\tilde{I}(\tau)$ on an equally spaced grid with N_{FFT} points and spacing $\delta\tau$, whose range and density are determined by the minimum and maximum values of w that we are interested in. In order to avoid boundary effects, we apply

---

[6]If ϕ is made smooth a GO image forms, but it satisfies $\mu \to 0$ in the singular limit (e.g., for the CIS [33]).

a Tukey window function to the time-domain signal. We extend τ towards negative values, such that the window function is $\simeq 1$ over all ϕ_I corresponding to GO images.

One difficulty is dealing with the discontinuities and singularities in $\tilde{I}(\tau)$ associated with GO images, as they produce components at arbitrarily high frequency. The discretization needed for the FFT causes aliasing of the frequencies $w > w_{\max}$, contaminating the computed signal at high w [Fig. 2(d)].

To avoid numerical artifacts it is convenient to treat the contribution of stationary points separately [29]. Hence, we split the integral into a regular and a singular part,

$$\tilde{I}(\tau) = \tilde{I}_{\text{reg}}(\tau) + \sum_J \tilde{I}_{\text{sing}}^J(\tau). \tag{36}$$

The left-hand side is obtained by evaluating Eq. (32) numerically, as described above. The singular contributions have closed-form expressions, which we give below. The WO amplification factor follows by Fourier transforming

$$F(w) = F_{\text{reg}}(w) + \sum_J F_{\text{sing}}^J(w). \tag{37}$$

The regular contribution is the FFT from $\tilde{I}_{\text{reg}}(\tau)$. The singular contributions are the GO amplification factors for each image [Eq. (6)] or are related to them. Note that the above splitting is arbitrary and valid as long as the time- and frequency-domain terms are consistent. Therefore, we can add any such terms in order to make the computation more robust. We now discuss these terms for different types of critical points.

Type I/III images (minima/maxima of the Fermat potential) correspond to discontinuities in $\tilde{I}(\tau)$. In this case,

$$\tilde{I}_{\text{sing}}^M(\tau) = 2\pi|\mu_J|^{1/2}\theta(\pm(\tau - \phi_J)), \tag{38}$$

where θ is the Heaviside step function and $+/-$ corresponds to a minimum/maximum with time delay ϕ_J. The corresponding GO contribution reads

$$F_{\text{sing}}^M(w) = \mp|\mu_J|^{1/2}e^{iw\phi_J}. \tag{39}$$

The discontinuity is interpreted as a family of contours ceasing to exist at the extremum. In the case of a cusp ($x \to 0$ in the SIS and gSIS), the contour ceases to exist but no discontinuity forms because $\mu_J = 0$.

A type II image (saddle point) with time delay ϕ_J produces a logarithmic divergence in $\tilde{I}(\tau)$ [29],

$$\tilde{I}_{\text{sing}}^S(\tau) \simeq -2|\mu_J|^{1/2}\log|\tau - \phi_J| + C, \tag{40}$$

where C is an integration constant. This calculation assumes that the quadratic approximation around the saddle

point, $\phi \simeq (\Delta x_1/a)^2 - (\Delta x_2/b)^2$, is valid for arbitrarily large separations Δx.[7] The corresponding GO contribution reads

$$F_{\text{sing}}^S(w) = i|\mu_J|^{1/2}e^{iw\phi_J}. \tag{42}$$

This term contributes at arbitrarily large values of τ, causing spurious low-frequency behavior upon FFT. One can avoid this issue by windowing the singular contribution $\tilde{I}_{\text{sing}}^S(\tau) \to W(\tau, T)\tilde{I}_{\text{sing}}^S(\tau)$ in Eq. (40). Choosing

$$W(\tau, T) = e^{-|\tau - \phi_J|/T} \tag{43}$$

preserves the singular behavior and avoids the low-frequency problems if $\delta\tau \ll T \ll \delta\tau N_{\text{FFT}}$, where N_{FFT} is the number of sampled points.

This choice produces a closed-form expression for the frequency domain,

$$F_{\text{sing}}^S(w, T) = \frac{-iw}{\pi}|\mu_J|^{1/2}e^{iw\phi_J}(\mathcal{I}_+ + \mathcal{I}_-), \tag{44}$$

where

$$\begin{aligned}\mathcal{I}_\pm(w, T) &\equiv \int_0^\infty dt \log(t)e^{-t/T \pm iwt} \\ &= \frac{-iT}{i \pm wT}(\gamma_E + \log(T^{-1} \mp iw)). \end{aligned} \tag{45}$$

Note that $\lim_{T\to\infty} \mathcal{I}_\pm = \mp\frac{i}{w}(\gamma_E + \log(w) \mp i\frac{\pi}{2})$, recovering Eq. (42).

Figure 2(c) shows the integral in the time domain, including both the regular and different singular contributions. Figure 2(d) shows the different contributions to $F(w)$: at low frequencies the singular part (corresponding to GO predictions) is compensated by the regular contribution and recovers the low-frequency limit $F(w \to 0) \to 1$. Without splitting the singular part, $F(w)$ loses precision at high frequencies and eventually becomes unreliable (solid gray line).

After the regularization, discontinuities remain in derivatives of $\tilde{I}(\tau)$ at the critical points $\tau = \phi_J$. When Fourier transformed, a discontinuous $\frac{d}{d\tau}\tilde{I}(\tau)$ corresponds to corrections $\propto 1/w$ in the amplification factor. These terms are

---

[7]Including only a finite region around the saddle point yields

$$\tilde{I}_{\text{sing}}^S(\tau) = 4|\mu_J|^{1/2}\cosh^{-1}\left(\sqrt{\frac{\delta\tau}{|\tau - \phi_J|}}\right), \tag{41}$$

where $\delta\tau$ defines the limit of the contour around the saddle point. Equation (40) follows when $\frac{\delta\tau}{|\tau - \phi_J|} \gg 1$. We do not use the more accurate Eq. (41), as it does not have a closed-form Fourier transform.

precisely the bGO and cusp contributions discussed in Sec. III A. Discontinuities extend to any derivative $\frac{d^n}{d\tau^n}\tilde{I}(\tau)$, with corresponding corrections $\Delta F^{(n)} \propto w^{-n}$ as higher-order bGO terms. Numerically, the discontinuous derivatives cause aliasing in the FFT and are a source of error, although the scaling with w makes these terms subdominant in the computation of $F(w)$ (see discussion in Sec. VI A). Eventually, our regularization method could be extended to split discontinuities in derivatives of $\tilde{I}(\tau)$ as higher precision is required.

Finally, let us mention that computing derivatives of the amplification factor accurately requires handling discontinuities in $\frac{d}{d\tau}\tilde{I}(\tau)$. This is because an additional derivative (e.g., with respect to the lens parameter Θ) promotes the w^n terms in F to $\sim w^{n+1}$ in $dF/d\Theta$; our regularization removes $\sim w$ terms, but leaves terms $\sim w^0$, which contribute significantly to aliasing. As computing derivatives of $F(w)$ is important in some applications of WO lensing (e.g., Fisher-matrix forecasts [33]), we discuss a workaround in the Appendix.

V. COMPLEX DEFORMATION

Another method to improve the convergence of the diffraction integral (1) relies on analytically continuing the integration variable into the complex plane. We follow a variation of the procedure described in Ref. [31] (see also Refs. [46–48]). Initially, we briefly review how to obtain a good integration contour in the complex plane for highly oscillatory 1D integrals. Then, we generalize the discussion to the more relevant case of 2D diffraction integrals with nonanalytic features, such as those that appear in gravitational lensing.

A. Flow of the integration domain

To outline the method, we start with a prototypical oscillatory integral, which resembles Eq. (1) in one dimension,

$$F(w) = \int_{-\infty}^{+\infty} dx\, g(x) e^{iwf(x)}, \qquad (46)$$

where $f(x)$ and $g(x)$ are assumed to be analytic in the full complex plane $z = x + iy \in \mathbb{C}$.[8] (Later, we will mention how to deal with possible branch cuts or poles away from the real line.) Clearly, the limit of large w corresponds to the saddle-point, or GO, approximation for Eq. (46).

---

[8] The distinction between $f(x)$ and $g(x)$ is ambiguous in Eq. (46). To partially fix the ambiguity, we assume that the convergence properties of the integral at infinity are solely determined by $f(x)$. As we are going to elaborate, convergence is established by deforming the integration contour into the complex plane [in particular, by tilting the contour above or below the real line, depending on the properties of $f(x)$].

(When dealing with complex functions, critical points can only be saddles.)

First, let us recall how to make sense of this type of oscillatory integrals, which are not manifestly convergent (see e.g., Ref. [49] for more details on this procedure). The integral (46) can be extended to the complex plane $z = x + iy$ by deforming the contour of integration away from the real line (because of Cauchy's theorem the final answer does not change). In particular, the contour can be decomposed into so-called steepest-descent paths, each associated with a saddle point. (Some saddles might be irrelevant in this decomposition and neglected, as they are not encountered when moving the real-line integration contour into the complex plane). The steepest-descent path $z(\lambda)$ of the function $f(x)$ associated with an isolated and nondegenerate saddle z_c [i.e., $f''(z_c) \neq 0$] satisfies the flow equation

$$\frac{d}{d\lambda} z(\lambda) = i \frac{\partial f^*}{\partial z^*}, \qquad (47)$$

where $\lambda \in \mathbb{R}$ parametrizes the path and z^* is the complex conjugate of z. From the equation above, it follows that

$$i \frac{d}{d\lambda} f = i \frac{\partial f}{\partial z} \frac{dz}{d\lambda} = -\left| \frac{\partial f}{\partial z} \right|^2. \qquad (48)$$

Therefore, the real part of the exponent of the integrand (46) monotonically decreases along the steepest-descent path: the integral is now manifestly convergent, as the integrand decays exponentially.[9] On the other hand, the imaginary part of the exponent remains constant along the curve $z(\lambda)$. Additionally, the saddle point z_c is reached only asymptotically in the flow. [At z_c the flow in Eq. (47) stops, as $f'(z_c) = 0$.]

The flow equation (47) can also be directly used to *determine* the integration contour, without needing to identify the relevant saddle points beforehand. This procedure, introduced in Ref. [31] and discussed below, is what we use in our applications. We start by considering again Eq. (47). In this flow equation we now impose as an initial condition at $\lambda = 0$ that $z(0) = x$, where x is a generic point on the initial integration contour $\mathcal{C}_{\lambda=0}$. [In the case of Eq. (46), $\mathcal{C}_{\lambda=0} = \mathbb{R}$.] Let us call $\mathcal{C}_\lambda$ the set of points $z(\lambda)$ at the "time" λ. As a result of Morse theory, the contour $\mathcal{C}_\lambda$ for $\lambda \to \infty$ converges to a steepest-descent contour. [Equation (47) represents a smooth deformation of the initial path $\mathcal{C}_{\lambda=0}$.] Therefore, just by repeat use of Eq. (47) for all of the points of the initial domain of integration, we can write the original integral for large enough λ as

$$F(w) = \int_{\mathcal{C}_\lambda} dz\, g(z) e^{iwf(z)}, \qquad (49)$$

---

[9] Together with the steepest-descent path, each saddle has an associated steepest-ascent path. We do not discuss these paths here, as they are unimportant for our discussion.

where the exponent is now real (up to a z-independent imaginary part) and not oscillatory. Standard numerical techniques can now be applied to this integral. Notice that C_λ does not depend on w, and therefore the path needs to be computed only once. This property applies to GW lensing, where w appears only linearly in the exponent. In a situation where the Fermat potential depends on the frequency, such as for wave diffraction in dispersive media, this is no longer the case.

B. Extension to realistic lenses

The procedure just outlined can be generalized to higher dimensions and applies to the diffraction integral (1). For our practical purposes, however, it is simpler to reduce $F(w)$ to a set of 1D integrals and apply the procedure above. To achieve this, we first write the integral over $\boldsymbol{x}$ in polar coordinates x and θ as

$$F(w) = \frac{w}{2\pi i} \int_0^{2\pi} d\theta \int_0^{+\infty} dx\, x e^{iw\phi(x,\theta,\boldsymbol{y})}. \quad (50)$$

The integral over θ is over a finite range and can be performed with standard numerical techniques. On the other hand, the integral over x is highly oscillatory and is suitable for the analytic continuation procedure. The contour-deformation method has to be applied for various values of θ, until the sampling of points is dense enough to guarantee numerical convergence.

The only difference with Eq. (46) is the lower limit of integration, which stops at $x = 0$. In order to apply Cauchy's theorem, the initial and final contours $C_{\lambda=0}$ and C_λ must close (up to a semicircle at large $|x|$, which is negligible). However, if the point $z(0) = 0$ is evolved according to the flow, it will in general move away from the origin, thus leaving the sum of the initial and final contours open. To avoid this issue, we decide to alter the flow equation (47) in such a way as to force the points close to the origin to not evolve. To do so, we rescale the flow variable $\lambda \to h_{z_0}\lambda$, where h_{z_0} is a function that depends on the initial position $z_0 \equiv z(0)$. Note that changing the flow equation does not modify the final result due to Cauchy's theorem. The flow equation then becomes

$$\frac{d}{d\lambda} z(\lambda) = i \frac{\partial f^*}{\partial z^*} h_{z_0}. \quad (51)$$

For convenience we choose h_{z_0} to be $h_{z_0} = \theta_\varepsilon(z_0 - \delta)$, where $\theta_\varepsilon(x) \equiv \frac{1}{2}[\tanh(x/\varepsilon) + 1]$ is smooth, and converges to the Heaviside step function for $\varepsilon \to 0$. The function h_{z_0} interpolates between $h_{z_0} \simeq 0$ for points $z_0 < \delta$ and $h_{z_0} \simeq 1$ for $z_0 > \delta$. The parameter ε sets how sharp the transition is. In the applications in the following sections we set $\varepsilon = 10^{-3}$ and $\delta = 10^{-2}$.

An additional complication arises when considering realistic lenses, which typically feature nonanalytic lensing

potentials. (Even the simplest example, the point lens $\psi = \log x$, has a branch cut.) Fortunately, our procedure is not significantly altered as long as we are dealing with branch cuts (and possibly poles, but we are not going to encounter them in our lensing models). Away from the branch cut the exponent is analytic, and the flow equation can be applied without modifications. However, it is possible that some points are driven towards the branch cut during the flow. In such cases, to avoid them crossing the cut, we decide to stop the flow. This can be implemented case by case (depending on the location of the cuts) by modifying the flow. Thus, we multiply the right-hand side of Eq. (51) by a function $b(z(\lambda))$ with the requirement that for $z(\lambda)$ approaching the cut, $b(z(\lambda)) \to 0$ smoothly, while $b(z(\lambda)) \simeq 1$ everywhere else. For the case of a point lens we have a branch cut for $\mathrm{Re}\, z < 0$. Following the same logic as for h_{z_0}, with this lens we choose $b(z) = 1 - \theta_\varepsilon(\varphi - \pi_\delta) - \theta_\varepsilon(-\varphi - \pi_\delta)$, where z is written in polar coordinates $z = re^{i\varphi}$ and we defined $\pi_\delta \equiv \pi - \delta$. With this choice, the evolution of the contours is halted as φ approaches $\pm\pi$. For the function $b(z)$, in the next section we will use the values $\varepsilon = 1/200$ and $\delta = 10^{-1}$.

Since we are modifying the flow equation, some of the nice properties of Eq. (47) are partially lost. In particular, it will no longer be true that the imaginary part remains constant along the final contour C_λ (ad hence some mild oscillations can reappear). In practice, for the cases we consider, this is not an issue since the modifications only affect the contour close to the origin, while leaving the behavior at large $|z|$ unaffected. (The convergence properties of the integral are thus preserved.)

We also notice that the integration contour at infinity converges to the 45-degree line $\arg x = \pi/4$, $\mathrm{Re}\, x > 0$. (For large x, the Fermat potential is dominated by its quadratic part.) The contour is however deformed as x approaches the origin, due to the lensing potential. Therefore, the method outlined in this section generalizes Eq. (16) and optimizes the choice for the contour.

Let us see how this procedure is applied in a particular lens model: the SIS lens. First, we fix a value for the angular variable θ in Eq. (50). We take it to be $\theta = \pi/4$ in this example [Fig. 3(a)]. Then, we evolve the integration contour from the positive real line $x > 0$ to the complex plane. Since this lens model does not introduce branch cuts or poles, the evolution of the path is obtained using Eq. (51). Then, it is stopped at some given flow time $\lambda = T$ and the path is truncated at some large value of $|x|$. The evolution of the paths is shown in Fig. 3(b). We can notice that all of the paths cross the real line at a fixed location; this corresponds to a saddle point of the exponent in Eq. (50). (However, this is different from the saddles corresponding to the GO approximation, since we are fixing θ here.) Once the paths are obtained, we can evaluate the integrand in Eq. (50) (which we call $\mathcal{F}$) on each path. This quantity is now also a function of w. As an example,
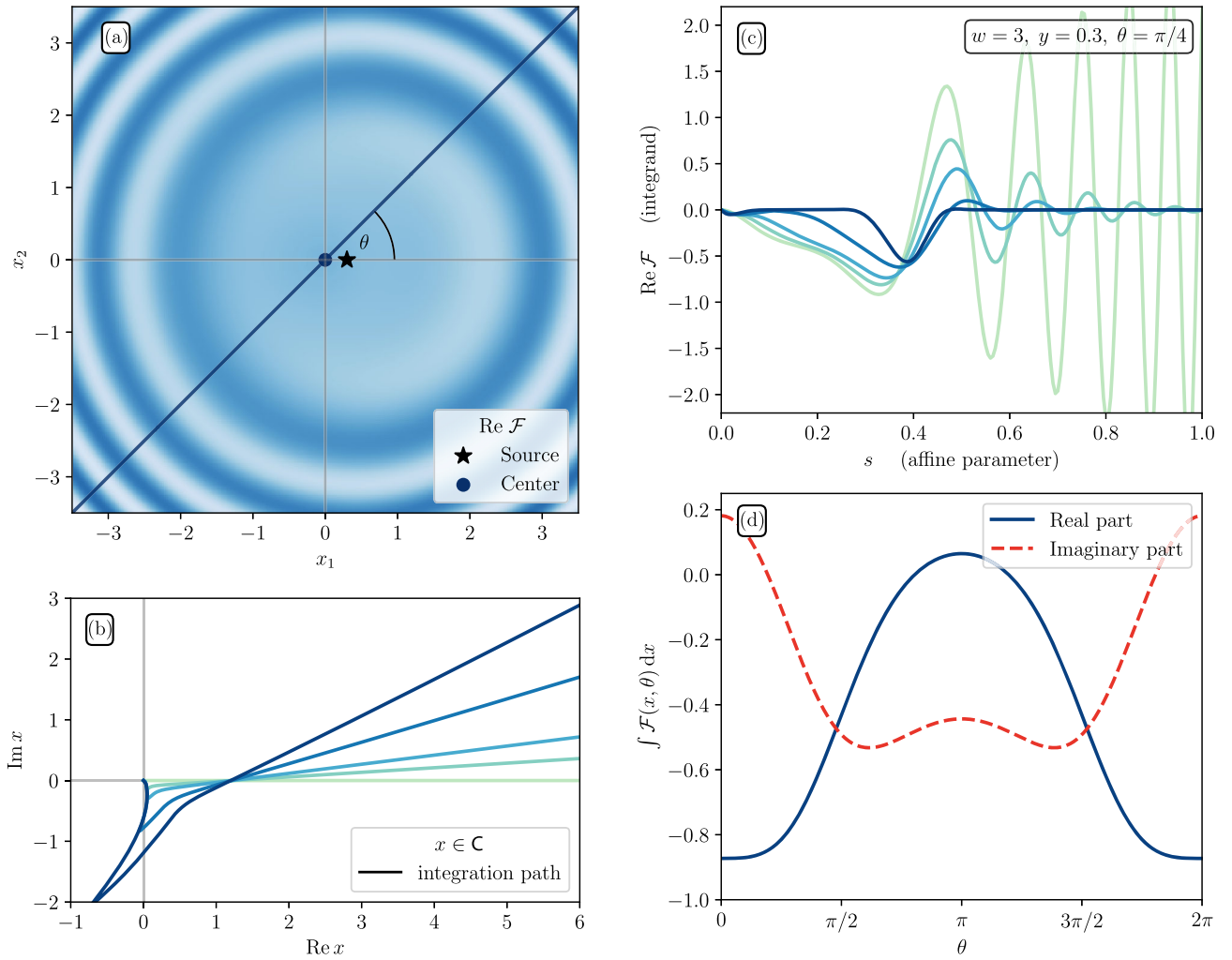
FIG. 3. WO lensing via the complex-deformation method. The lens is a SIS with $y = 0.3$ and fixed $w = 3$. Panel (a): the integrand $\mathcal{F}$ in Eq. (50) (shown in the density plot) is highly oscillatory in the lens plane. First, we select a value for the angle θ in the lens plane (blue line) where the flow equation is then applied; for this example, we choose $\theta = \pi/4$. Panel (b): evolution of the integration path under the flow equation (51), starting from the positive real line $x > 0$ (light green line). Darker lines are obtained by increasing λ in the flow. Panel (c): the integrand at fixed θ evaluated on the paths of panel (b) (as an example, only the real part of $\mathcal{F}$ is shown). We use the affine parameter s, which parametrizes each path, as the x axis. The initial integration contour $\lambda = 0$ gives large oscillations that are difficult to treat numerically. For $\lambda > 0$ the integrand becomes exponentially damped very quickly at large s. Panel (d): integral over the complex variable x as a function of the angle θ, obtained by repeating the steps from panels (a)–(c) for different θ's. The amplification factor in Eq. (50) is then obtained by integrating over θ; the latter integration has no convergence problems.

we show $\mathcal{F}$ for fixed w and θ in Fig. 3(c). Clearly, the problematic oscillations in $\mathcal{F}$ get damped very quickly as the flow progresses. For large values of λ the integral becomes very localized around the saddle point. Finally, one has to repeat the steps A–C for different values of θ. The integral of $\mathcal{F}$ over x as a function of θ is shown in Fig. 3(d); for moderate w, this function is not oscillating too rapidly and can be integrated easily.

In the results presented in the following sections, we use the following settings for the complex-deformation method. The contours are evaluated for $n_1 = 25$ values of θ, uniformly distributed between 0 and 2π (for symmetric lenses one can limit to the range 0 to π).

The integrand is then sampled over a larger number of values of θ, $n_1 \cdot n_2$, with $n_2 = 25$. We can sidestep evaluating $n_1 \cdot n_2$ contour flows because the final integral is independent of the choice of the contour. Therefore, for a given angle, we use the contour evaluated with the nearest value of θ.

For the flow of each contour, we sample the initial contour along $x > 0$ with $n_x = 340$ points, not uniformly distributed but concentrated towards $x = 0$. The flow equation is implemented in Python, using the odeint function of the SciPy package on default settings. After applying the flow equation, the final contour is interpolated over $n_x^{\text{interp}} = 1000$ points.

VI. ACCURACY AND PERFORMANCE

We now discuss the accuracy of the algorithms described in Secs. IV and V and their convergence to systematic expansions (Sec. III). We first compare the results for a point lens (Sec. VI A) and then against each other (Sec. VI B) for the other axially symmetric lenses in Table I. We end by discussing the performance of the different methods (Sec. VI C). All of the comparisons are made with the impact parameter $y = 0.3$; similar conclusions are reached for different values of y, sufficiently far from caustics. The precision parameters used in the contour method are summarized in Table II.

A. Comparison to point lens

In order to assess the goodness of our numerical methods, we can compare to the point-lens model [$\psi(x) = \log x$], where the diffraction integral is known analytically [see Eq. (20)].

We compare the result from the contour method of Sec. IV and the complex-deformation method of Sec. V with Eq. (20) for $y = 0.3$ in Fig. 4, where the results of GO and bGO are also reported. The contour method is most accurate in the intermediate-w regime, up to $w \sim 10$, while
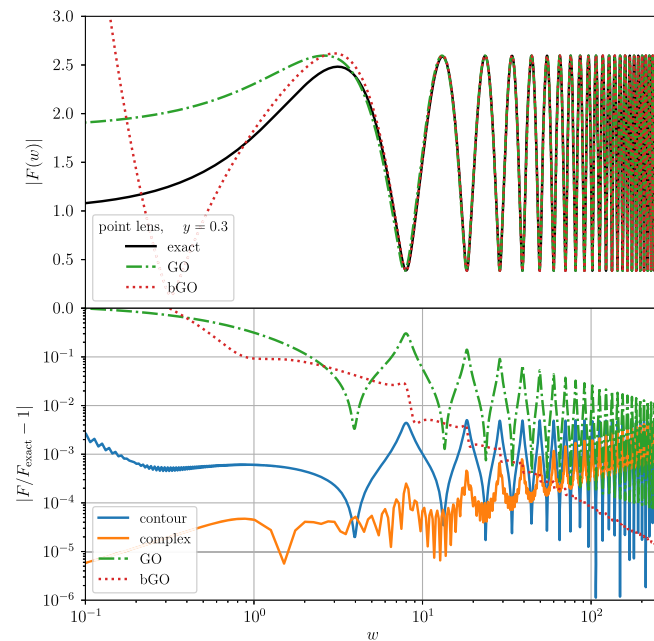
FIG. 4. Method comparison for a point lens ($y = 0.3$). Top: absolute value of the amplification factor $|F(w)|$. The contour and complex method are not shown explicitly, as they overlap with the exact solution. Bottom: differences relative to the exact solution. The contour method (blue) always performs at the subpercent level, while the complex-deformation method (orange) at low frequencies is around 1 order of magnitude better. The GO approximation (light green) converges very quickly, remaining subpercent for $w > 10$, whereas the bGO approximation (red) converges even faster.

the complex-deformation method remains good even at $w \sim 10^2$.

Let us now discuss the comparison with the contour method more in detail, since it will be the primary method used in future applications [33]. We will discuss the complex-deformation method's performance in the following subsection. At low frequencies ($w \lesssim 0.1$) the numerical result from the contour method stops being accurate. This is related to the way that the numerical calculation is performed. Indeed, the signal is obtained through a Fourier transform from the time-domain signal $\tilde{I}(\tau)$. Therefore, the low-frequency errors are related to the numerical truncation of the integral in Eq. (32) for large time delays, which depends on the windowing of $\tilde{I}(\tau)$. Higher precision can be achieved at low frequencies by extending the integral (32) to larger τ's, at the expense of making the numerical evaluation slower.

In the opposite regime, for large w, we also lose accuracy. The appearance of error in this regime can be understood in the following way. At high w, the signal can be written as follows:

$$F(w) = F_{\text{reg}}^{(n_{\max})}(w) + \sum_{J,n}^{n_{\max}} \frac{c_n^{(J)}}{w^n} F_{\text{GO}}^J(w), \qquad (52)$$

where the sums are over the different images J and the higher-order GO corrections that scale as $\sim w^{-n}$. Here, for $n = 0$ we recover GO ($c_0^{(J)} = 1$) and for $n = 1$ we instead have bGO ($c_1^{(J)} = i\Delta_J$). The term $F_{\text{reg}}^{(n_{\max})}(w)$ represents the regular WO contribution, not captured by the GO up to order $n_{\max}$. We can notice that all of the GO terms, when Fourier transformed to the time domain τ, give some "singular" features. In particular, for $n = 0$, as we already discussed in Sec. IV B, we can have θ-function discontinuities or log divergences in $\tilde{I}(\tau)$. As discussed there, there are also discontinuities/singularities in the nth derivative of $\tilde{I}(\tau)$ with respect to τ, for any n. Due to finite numerical accuracy, such sharp features pollute the signal at arbitrarily high w when transformed back to frequency space. Having understood this, we have a strategy for potential future improvements in the accuracy of our code. Indeed, these additional GO contributions could be subtracted before performing the inverse Fourier transform, in the same spirit as what was already done in the case of $n = 0$. By performing this procedure up to $n = n_{\max}$, we expect the residuals against the full result to scale as $\sim 1/w^{1+n_{\max}}$. Of course, other sources of error might then become dominant. We expect that these remarks also apply to other lens models.

B. Comparison between methods

Here we compare the numerical results from the contour method and the complex-deformation method introduced in Secs. IV and V, respectively. Again, we consider the extended lenses described in Table I.
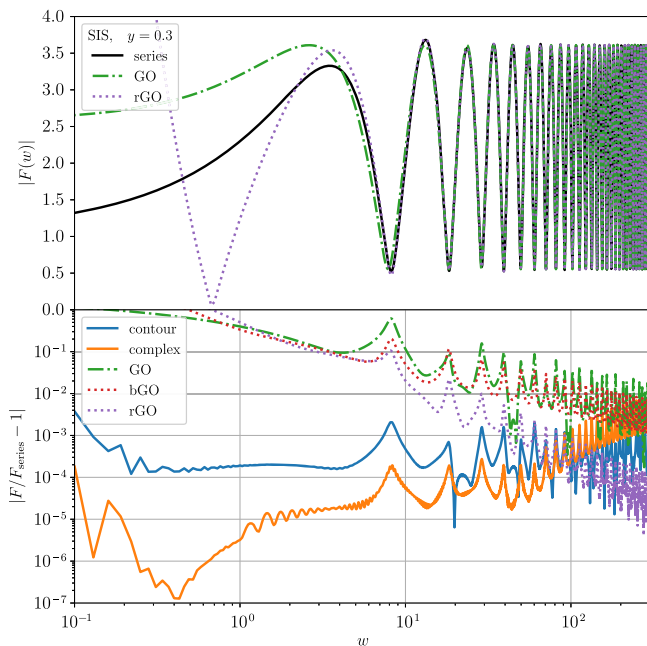
FIG. 6. Comparison between methods for a gSIS lens, where F_{series} is the series expansion of Eq. (29) truncated at some adequate n, as for the SIS case in Fig. 5. Instead of the usual bGO approximation, here we compare against the rGO approximation of Eq. (15) (red). The performance is overall very similar to the SIS case.

FIG. 5. Method comparison for the SIS ($y = 0.3$). Top: absolute value of the amplification factor $|F(w)|$. F_{series} is the series expansion of Eq. (30). The contour and complex method overlap with it and are not shown. Bottom: difference relative to the series solution. In the WO regime both the contour and complex-deformation methods perform below the per-mille level. The GO approximation converges to below percent level for $w \gtrsim 100$ and the bGO does not substantially improve convergence. The inclusion of the cusp information (rGO) gives a much faster convergence instead.

For the SIS lens, as we have discussed in Sec. III B 2, a series representation for the integral is available and can be used for comparison with our numerical methods. A comparison with the series (30) is shown in Fig. 5, again for $y = 0.3$. We can see that the agreement for both of our numerical methods is below the per-mille level in the range $10^{-1} \lesssim w \lesssim 10$.

At low frequencies the contour method starts to fail, as seen from the nonsmooth curve for F. On the other hand, the complex-deformation method works best in this regime. It is more accurate since the (typically oscillatory) angular integral over θ in Eq. (50) is not particularly computationally demanding.[10] Going instead to higher w reverses the situation: the complex-deformation method becomes slower and is outperformed by the contour one. The main reasons are the increasing oscillations in the angular integral and the fact that the computation has to be

performed frequency by frequency (the contour method instead evaluates F directly at all frequencies).

In our code, the accuracy of the complex-deformation method can be improved by increasing the sampling of the path C_λ and the integral over θ. This is at the cost of a longer evaluation time.

Let us compare different methods for computing the gSIS amplification factor. We test the analytic result of Eq. (29) against the contour and complex-deformation methods. Additionally, we also check the improvement of the rGO approximation of Eq. (15) against the GO-only result. The results are shown in Fig. 6. As we can see, the general results found for the SIS lens in Fig. 5 are preserved here, with similar orders of magnitude for the accuracy against the analytical result. Also, we can notice the slightly better agreement between the rGO compared with only GO. (The bGO curve, which is not shown, gives a similar residual as the GO one.) With these results, we can establish that the contour and complex-deformation methods are accurate enough to study the gSIS lens.

The final lens we consider is the CIS. In this case, as already discussed in Sec. III B 2, a series representation is not available. Therefore, in Fig. 7 we compare the complex-deformation method against the contour method directly. Moreover, comparisons with the GO and bGO results are also shown. As we can see, the two numerical methods have the lowest residuals around $w \sim 1$, while at lower and higher frequencies the results degrade. As for the other lenses, at low w the contour method loses accuracy. At higher frequencies, the complex-deformation method instead becomes less reliable, making the residual bigger. We can notice that the trends are very similar to those of Figs. 5 and 6 for the SIS and gSIS lenses. In comparing against GO and bGO, we find similar features as for other

---

[10]In the SIS case in Fig. 5, we start noticing a loss in accuracy when moving towards lower w's. This is because for small w the integrand in Eq. (49) has support for large values of $|z|$ along the contour path C_λ. Since we truncate the path to a finite range, we effectively lose part of the integration domain. The problem is however straightforward to correct.
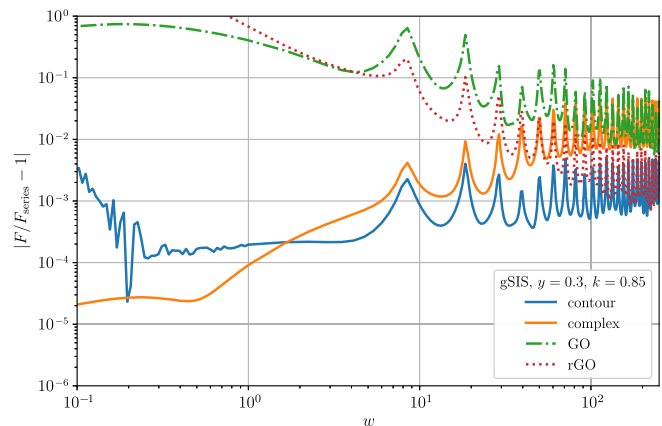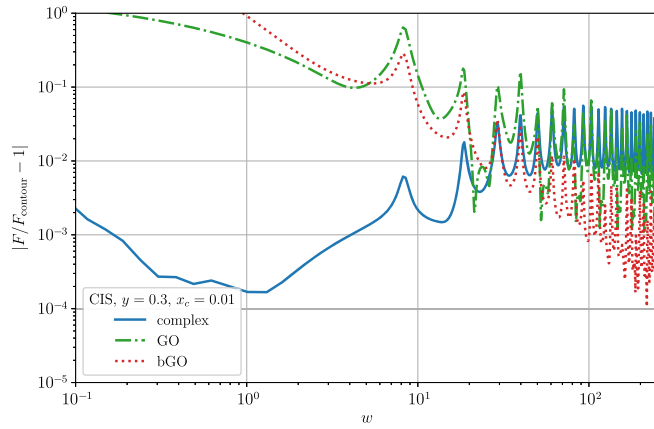
FIG. 7. Comparison between methods for a CIS lens, where in this case the reference is taken to be the contour method $F_{contour}$. (For CIS there is no explicit series representation for the amplification factor known to us.) The performance is similar to the point-lens case, with the GO and bGO methods becoming very reliable after $w > 10$.

FIG. 9. Comparison between the low-w expansion F^{CIS} of Eq. (28) and the complex-deformation method of Sec. V for a CIS lens with $y = 0.3$. Different curves correspond to different values of the core size x_c. The analytic expansion reaches per-mille accuracy for $w \lesssim 10^{-2}$, while the expansion breaks down around $w \sim 1$, as expected.

lenses; as expected, the residuals scale as $\sim 1/w$ and $1/w^2$, respectively. From this observation, we can argue that the contour method remains accurate below the percent level for $1 \lesssim w \lesssim 300$, at least. If this was not the case, the residual with respect to GO and bGO would saturate at high frequencies. For CIS there is no rGO curve, as the center of the lens is regular and there is no cusp contribution.

We also tested our results with different impact parameter values, obtaining similar agreements between methods. However, accuracy degrades as we approach a caustic where two images merge. Since images are closer in this situation, a lower precision is expected; resolving them requires higher resolution in the time delays (for the contour method) and higher resolution in the image plane (complex-deformation method). In the case of the CIS, a
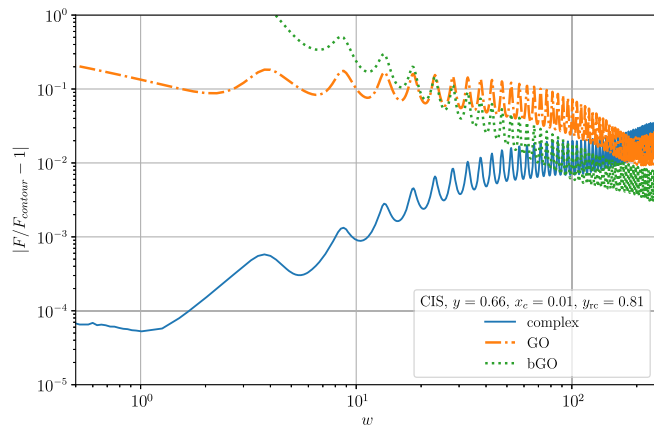
caustic occurs at an impact parameter y_{rc}. [See Eq. (64) in Ref. [33] for the explicit expression.] A comparison at a larger impact parameter is shown in Fig. 8.

For SIS and gSIS lenses, the series representations [Eqs. (29) and (30), respectively] reduce to the low-w expansions [Eqs. (24) and (26)] for small enough w. Therefore, the comparisons against the numerical methods in Figs. 5 and 6 implicitly show the goodness of this approximation. To perform a similar test for the CIS lens, we compare the low-w expansion (28) against the complex-deformation method in Fig. 9. The low-frequency approximation performs at the subpercent level for $w \lesssim 10^{-1}$, while per-mille accuracy is reached for $w \lesssim 10^{-2}$. Notice that the contour method would lose accuracy in this region. These results have a mild dependence on the value of x_c, with more accurate results for larger x_c.

C. Performance

The contour method is by far the fastest computationally. Our implementation in Python (optimized with Numba, after precompiling) computes $F(w)$ in the range $w_{min} \sim 0.01, w_{max} \sim 1000$ on a 12-core laptop (i7-10750H CPU) in 323 ms, a range similar to the one used for Figs. 4–7.[11] (The numbers refer to the point lens, and the extended lenses require similar execution times.)

The contour method is faster than computing the exact solution for the point lens (20): it takes 5.1 s on the same machine sampling the same range of w over 10^4 points (a factor of $1/10$ fewer values of w than quoted

FIG. 8. Comparison between methods for a CIS lens, as in Fig. 7 but with a larger impact parameter $y = 0.66$, closer to the caustic $y_{rc} = 0.81$. In this case the accuracy degrades, but remains of order 1% for $w < 100$.

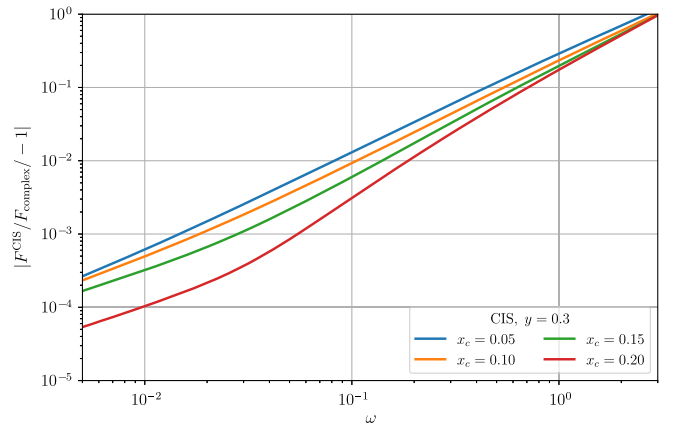[11]This corresponds to $2^{17} \sim 10^5$ points in the FFT; increasing the number of points ($\propto w_{max}/w_{min}$) slows the computation due to the interpolation and FFT.

above). A single evaluation of the exact solution (20) takes 0.47 ms at $w \sim 0.01$ and 5.7 ms at $w \sim 1000$.

GO and bGO calculations are very inexpensive, requiring 12 and 15 ms for the same lens, respectively. Because the contour method employs regularization, the GO amplification factor is already computed.

Complex deformation is efficient at low w but each dimensionless frequency needs a separate computation. Moreover, the angular integral becomes highly oscillatory for large w and needs to be sampled very finely to obtain the desired accuracy, at the cost of increasing the evaluation time considerably. With this method, one first needs to evolve the contours of integration [Fig. 3(b)] through the flow equation for different values of the angle θ. This evaluation takes around $\sim$300 ms for a single angle and 100 points on the x integration path. Parallelization can be used to speed up the evaluation over multiple angles (for $\sim$50 values of θ the overall evaluation takes $\sim$a few s). After this step, the evaluation of $F(w)$ at a single value of w takes around $\sim$300 ms. Most of the computational time is spent evaluating the integrand function over the 2D domain of integration. Evaluation over multiple w's is then parallelized, which generally provides a factor $\sim$5 gain in speed. The situation worsens if w is increased too much since the number of sampled angles θ needed for a precise evaluation has to increase (the timing will scale almost linearly with the number of angles).

Given the different execution times between both methods, employing the contour method in applications such as parameter estimation for GWs is more convenient. The complex-contour method remains a valuable tool for the validation of our results, in particular at low frequencies. For instance, it allows us to test the low-w behavior derived in Sec. III B for different lens models.

VII. CONCLUSIONS

In this work we have developed, implemented, and validated methods to compute gravitational lensing predictions in the WO regime. We first outlined the general framework for WO computations and introduced several lenses that serve as examples for comparison (Sec. II). We described systematic expansions valid at high and low frequencies (Sec. III). The GO expansion is valid for $w \propto GM_{Lz}f \rightarrow \infty$ (Sec. III A). It gives the amplification as a sum over images, each of which carries a magnification, time delay, and Morse phase. Finite frequency corrections $\propto 1/w$ can be systematically included, with terms that depend on derivatives of the lensing potential at the GO images. Similar $1/w$ corrections stem from nonsmooth features of the lensing potential, which are not associated with GO images and vanish at sufficiently high frequency.

While GO is a local expansion around critical points, a low-frequency expansion highlights the dependence on the lens' global properties and asymptotic behavior. The $w \ll 1$ limit (Sec. III B) allows us to explore the deep WO regime

and leads to simple expressions for our example lenses. The leading-order corrections depend on the asymptotic of the lensing potential, a trend clearly seen in the convergence towards free propagation $F \simeq 1$ as $w \rightarrow 0$:

(1) The point lens shows the fastest convergence, with $F - 1 \propto w + \mathcal{O}(w^2)$. This follows from $\psi \propto \log(x)$ being the slowest possible asymptotic growth of $|\psi|$.

(2) Extended lenses approach the unlensed case more slowly, as $F - 1 \propto w^{k/2} + \mathcal{O}(w^{k/2+1})$ for $\psi \propto x^k$, and $k < 2$ is needed to keep the enclosed mass finite.

This difference can be explained by the larger projected mass within a region of radius $\propto 1/w$, which dominates the diffraction integral at low frequencies. Hence, we expect that an extended but isolated lens (e.g., truncated at finite radius) will recover the point-lens convergence at sufficiently low w. The point-lens limit cannot be recovered by the gSIS, as it requires $k \rightarrow 2$, leading to a divergent mass.

While the low-frequency series can be computed, convergence requires including many terms, even at moderately high frequencies. Intermediate frequencies depend on the properties of the lensing potential across the lens plane, which are more efficiently computed numerically.

We developed and presented two numerical methods to compute WO lensing. The regularized contour-flow method (Sec. IV) solves the Fourier transform of the diffraction integral (1) by adaptively sampling equal-time contours of the Fermat potential. Subtracting the singular contributions and then adding their appropriate terms after transforming back to the frequency domain significantly reduces numerical noise at high frequencies. The complex-deformation method (Sec. V) analytically continues the integration variable in the complex plane. A well-defined process to flow the integration contour allows us to solve convergent, nonoscillatory integrals.

Both methods are complementary to each other. The method of contour flow allows a very fast computation of the amplification factor over a whole range of frequencies using FFT. The computation is efficient enough for GW parameter estimation with LVK data, although further optimization might be necessary to study complex lenses described by many parameters. A main shortcoming of contour flow is that it requires knowing the initial and final conditions for each contour. While the endpoints are solutions to the lens equation, setting up a calculation for a complex setup with many images can become very involved. In contrast, complex deformation does not require knowledge of solutions to the lens equation. However, the method is costly, as each value of w needs to be computed independently. Moreover, high frequencies require a very fine sampling of the angular integral. (This is not the case for contour flow, where one only needs to increase N_{FFT} to reach higher w.)

We performed the first cross-validation of these numerical methods for different lensing potentials. We can achieve subpercent accuracy over a broad range of frequencies with both methods. These results are optimal at intermediate

frequencies, and can be matched to analytic expansions whenever the method fails or becomes too costly. Besides comparing with the exact point-lens solution, we found excellent agreement with the series solution for the SIS and gSIS. Having two independent methods allows us to validate the predictions for lenses for which no systematic solution is known, as we demonstrated for the CIS. This will be important when considering more realistic and involved lens models.

Our main conclusions can be summarized as follows:

(1) High- and low-frequency limits capture different properties of the lens. The large-w limit depends on the critical points and nonanalytic features, while the low-w limit depends on the asymptotics of the lensing potential. Intermediate w requires knowledge of the entire lensing potential.

(2) Predictions in any regime can be obtained efficiently by combining numerical methods at intermediate frequencies with analytical approximations at low/ high frequency.

(3) We found subpercent agreement to exact solutions, as well as between different methods in their regime of validity. Subpercent accuracy holds for all of the lenses we considered without fine-tuning the precision parameters.

(4) Numerical methods offer complementary advantages: contour flow gives frequency-dependent predictions very quickly ($\lesssim 1$ s on a laptop). Complex deformation does not require prior knowledge of solutions to the lens equation.

(5) These methods offer insights into WO phenomena. Complex deformation is particularly useful for understanding the low-frequency limit. The contour method gives a transparent interpretation of GO and bGO (as nonanalytic features in the time-domain integral or its derivatives) and its splitting from other WO effects.

Our methods provide a baseline for computing gravitational lensing predictions in the WO regime. However, many improvements are possible and will be desirable in the near future. A clear direction will be the extension to more complex gravitational lenses. This requires allowing the methods to work with tabulated values for the lensing potential (rather than closed-form expressions), streamlining steps such as finding the limits of contours or the sampling of integrals in terms of precision parameters. A goal of this program is to make the methods available and integrate them into a public software tool [50,51]. We also envision further developments, such as including a robust computation of amplification factor derivatives to improve lens parameter inference. Our tools can also be generalized to other applications, such as plasma lensing [30,52], continuous GWs [53], studying GW polarization effects [54–56], and testing gravitational theories [57–60].

The subpercent accuracy we have demonstrated is sufficient for the near-term future of GW observations.

In particular, it allows us to model lensed waveforms by LVK and even third-generation GW observatories, where we expect signal-to-noise (SNR) ratios $\lesssim 100$. Higher accuracy might be possible by better adjusting the settings of our calculations, although refinements, such as including $1/w$ terms in the regularization scheme, will eventually become necessary. These improvements will eventually be required for analyzing higher SNR sources, such as massive black hole binaries (SNR $\sim 10^3$–10^4) that will be observed by LISA and other space-borne detectors. Now and in the future, these methods will facilitate many applications, from searching for WO effects in GW data to novel probes of the matter distribution in the Universe and fundamental physics.

APPENDIX: DERIVATIVES OF $F(w)$ VIA REGULARIZED CONTOUR FLOW

Let us outline how one can evaluate numerical derivatives with respect to the lensing parameters Θ_l of the WO amplification factor $F(w)$. This is relevant, for instance, in computing Fisher-matrix elements in a forecast for GW detectors.

We focus on the contour method since it is the most suitable for these applications. Here, $F(w)$ and its time-domain counterpart $\tilde{I}(\tau)$ are split into singular and regular parts [recall Eqs. (36) and (37)]. We can evaluate derivatives on the singular part easily in the frequency domain. (In the time domain, one instead needs to take the difference of singular functions, which is problematic.) The singular part only depends on the images, and we do not encounter problems when taking small numerical variations for the parameters Θ_l. On the other hand, derivatives of $F_{\mathrm{reg}}(w)$ can be computed in the time domain via finite differences and then Fourier transformed:

$$\tilde{I}_{\mathrm{reg},l}(\tau) \simeq \frac{\tilde{I}_{\mathrm{reg}}(\tau, \Theta_l + \epsilon) - \tilde{I}_{\mathrm{reg}}(\tau, \Theta_l)}{\epsilon}, \qquad (A1)$$

where $\tilde{I}_{\mathrm{reg},l}(\tau) \equiv \partial \tilde{I}_{\mathrm{reg}}(\tau)/\partial \Theta_l$. We chose ϵ so that $|\phi_J(\Theta_l + \epsilon) - \phi_J(\Theta_l)| < 1/f_{\mathrm{max}}$ for all images J, so the Fermat potential of all images varies less than the grid spacing used in the Fourier transform. Despite working with the regularized integrand, differentiating promotes discontinuities

in the derivatives (associated with bGO corrections) to discontinuities in the function. Numerical issues associated with these discontinuities can be ameliorated by further splitting as

$$\tilde{I}_{\text{reg},l} = \tilde{I}_{\text{reg},l}^{(2)} + \sum_J \Delta \tilde{I}_{\text{sing},l}^{(J)} \theta(\tau - \phi_J), \qquad (A2)$$

where $\Delta \tilde{I}_{\text{sing},l}^{(J)}$ is the discontinuity of the derivative of the regular part associated with the image J. Derivatives of the amplification factor $F(w)_{,l}$ are computed by adding the FFT of the regularized term $\tilde{I}_{\text{reg},l}^{(2)}(\tau)$ and analytic expressions for the Fourier transform of the step functions, cf. Eq. (39).

[1] M. Bartelmann, Gravitational lensing, Classical Quantum Gravity **27,** 233001 (2010).

[2] B. P. Abbott *et al.* (LIGO Scientific and Virgo Collaborations), Observation of Gravitational Waves from a Binary Black Hole Merger, Phys. Rev. Lett. **116,** 061102 (2016).

[3] R. Abbott *et al.* (LIGO Scientific, VIRGO, and KAGRA Collaborations), GWTC-3: Compact Binary Coalescences Observed by LIGO and Virgo During the Second Part of the Third Observing Run, arXiv:2111.03606 [Phys. Rev. X (to be published)].

[4] R. Abbott *et al.* (LIGO Scientific and VIRGO Collaborations), Search for lensing signatures in the gravitational-wave observations from the first half of LIGO–Virgo's third observing run, Astrophys. J. **923,** 14 (2021).

[5] L. Dai, B. Zackay, T. Venumadhav, J. Roulet, and M. Zaldarriaga, Search for lensed gravitational waves including morse phase information: An intriguing candidate in O2, arXiv:2007.12709.

[6] L. Dai, S.-S. Li, B. Zackay, S. Mao, and Y. Lu, Detecting lensing-induced diffraction in astrophysical gravitational waves, Phys. Rev. D **98,** 104029 (2018).

[7] M. Oguri, Strong gravitational lensing of explosive transients, Rep. Prog. Phys. **82,** 126901 (2019).

[8] R. Takahashi and T. Nakamura, Wave effects in gravitational lensing of gravitational waves from chirping binaries, Astrophys. J. **595,** 1039 (2003).

[9] P. Cremonese, D. F. Mota, and V. Salzano, Characteristic features of gravitational wave lensing as probe of lens mass model, Ann. Phys. (Amsterdam) **535,** 2300040 (2023).

[10] M. Çalışkan, L. Ji, R. Cotesta, E. Berti, M. Kamionkowski, and S. Marsat, Observability of lensing of gravitational waves from massive black hole binaries with LISA, Phys. Rev. D **107,** 043029 (2023).

[11] S. Savastano, G. Tambalo, H. Villarrubia-Rojo, and M. Zumalacarregui, Weakly lensed gravitational waves: probing cosmic structures with wave-optics features, arXiv:2306 .05282.

[12] P. Christian, S. Vitale, and A. Loeb, Detecting stellar lensing of gravitational waves with ground-based observatories, Phys. Rev. D **98,** 103022 (2018).

[13] J. M. Diego, O. A. Hannuksela, P. L. Kelly, T. Broadhurst, K. Kim, T. G. F. Li, G. F. Smoot, and G. Pagano, Observational signatures of microlensing in gravitational waves at LIGO/Virgo frequencies, Astron. Astrophys. **627,** A130 (2019).

[14] M. H. Y. Cheung, J. Gais, O. A. Hannuksela, and T. G. F. Li, Stellar-mass microlensing of gravitational waves, Mon. Not. R. Astron. Soc. **503,** 3326 (2021).

[15] A. Mishra, A. K. Meena, A. More, S. Bose, and J. S. Bagla, Gravitational lensing of gravitational waves: Effect of microlens population in lensing galaxies, Mon. Not. R. Astron. Soc. **508,** 4869 (2021).

[16] S. M. C. Yeung, M. H. Y. Cheung, J. A. J. Gais, O. A. Hannuksela, and T. G. F. Li, Microlensing of type II gravitational-wave macroimages, arXiv:2112.07635.

[17] S. Jung and C. S. Shin, Gravitational-Wave Fringes at LIGO: Detecting Compact Dark Matter by Gravitational Lensing, Phys. Rev. Lett. **122,** 041103 (2019).

[18] J. M. Diego, Constraining the abundance of primordial black holes with gravitational lensing of gravitational waves at LIGO frequencies, Phys. Rev. D **101,** 123512 (2020).

[19] M. Oguri and R. Takahashi, Probing dark low-mass halos and primordial black holes with frequency-dependent gravitational lensing dispersions of gravitational waves, Astrophys. J. **901,** 58 (2020).

[20] S. Basak, A. Ganguly, K. Haris, S. Kapadia, A. K. Mehta, and P. Ajith, Constraints on compact dark matter from gravitational wave microlensing, Astrophys. J. Lett. **926,** L28 (2022).

[21] J. Urrutia and V. Vaskonen, Lensing of gravitational waves as a probe of compact dark matter, Mon. Not. R. Astron. Soc. **509,** 1358 (2021).

[22] X. Guo and Y. Lu, Probing the nature of dark matter via gravitational waves lensed by small dark matter halos, Phys. Rev. D **106,** 023018 (2022).

[23] M. Oguri and R. Takahashi, Amplitude and phase fluctuations of gravitational waves magnified by strong gravitational lensing, Phys. Rev. D **106,** 043532 (2022).

[24] P. C. Peters, Index of refraction for scalar, electromagnetic, and gravitational waves in weak gravitational fields, Phys. Rev. D **9,** 2207 (1974).

[25] N. Matsunaga and K. Yamamoto, The finite source size effect and the wave optics in gravitational lensing, J. Cosmol. Astropart. Phys. 01 (2006) 023.

[26] R. Takahashi, Quasigeometrical optics approximation in gravitational lensing, Astron. Astrophys. **423,** 787 (2004).

[27] A. J. Moylan, D. E. McClelland, S. M. Scott, A. C. Searle, and G. V. Bicknell, Numerical wave optics and the lensing of gravitational waves by globular clusters, in *Proceedings of the 11th Marcel Grossmann Meeting on General Relativity* (World Scientific Publishing, Singapore, 2007), pp. 807–823, arXiv:0710.3140.

[28] X. Guo and Y. Lu, Convergence and efficiency of different methods to compute the diffraction integral for gravitational lensing of gravitational waves, Phys. Rev. D **102,** 124076 (2020).

[29] A. Ulmer and J. Goodman, Femtolensing: Beyond the semiclassical approximation, Astrophys. J. **442,** 67 (1995).

[30] G. Grillo and J. Cordes, Wave asymptotics and their application to astrophysical plasma lensing, arXiv:1810 .09058.

[31] J. Feldbrugge, U.-L. Pen, and N. Turok, Oscillatory path integrals for radio astronomy, Ann. Phys. (Amsterdam) **451,** 169255 (2023).

[32] D. L. Jow, U.-L. Pen, and J. Feldbrugge, Regimes in astrophysical lensing: Refractive optics, diffractive optics, and the Fresnel scale, arXiv:2204.12004.

[33] G. Tambalo, M. Zumalacárregui, L. Dai, and M. H.-Y. Cheung, Gravitational wave lensing as a probe of halo properties and dark matter, arXiv:2212.11960.

[34] P. Schneider, J. Ehlers, and E. E. Falco, *Gravitational Lenses* (Springer-Verlag Berlin, Heidelberg, 1992).

[35] C. R. Keeton, A catalog of mass models for gravitational lensing, arXiv:astro-ph/0102341.

[36] H. Gil Choi, C. Park, and S. Jung, Small-scale shear: Peeling off diffuse subhalos with gravitational waves, Phys. Rev. D **104,** 063001 (2021).

[37] G. Hinshaw and L. M. Krauss, Gravitational lensing by isothermal spheres with finite core radii: Galaxies and dark matter, Astrophys. J. **320,** 468 (1987).

[38] R. A. Flores and J. R. Primack, Cluster cores, gravitational lensing, and cosmology, Astrophys. J. Lett. **457,** L5 (1996).

[39] L. Dai and T. Venumadhav, On the waveforms of gravitationally lensed gravitational waves, arXiv:1702.04724.

[40] R. Blandford and R. Narayan, Fermat's principle, caustics, and the classification of gravitational lens images, Astrophys. J. **310,** 568 (1986).

[41] R. Takahashi, Wave effects in the gravitational lensing of gravitational waves from chirping binaries, Kyoto University, 2004, http://cosmo.phys.hirosaki-u.ac.jp/takahasi/dt.pdf.

[42] R. Takahashi, T. Suyama, and S. Michikoshi, Scattering of gravitational waves by the weak gravitational fields of lens objects, Astron. Astrophys. **438,** L5 (2005).

[43] T. Suyama, On arrival time difference between lensed gravitational waves and light, Astrophys. J. **896,** 46 (2020).

[44] J. M. Ezquiaga, W. Hu, and M. Lagos, Apparent superluminality of lensed gravitational waves, Phys. Rev. D **102,** 023531 (2020).

[45] T. T. Nakamura and S. Deguchi, Wave optics in gravitational lensing, Prog. Theor. Phys. Suppl. **133,** 137 (1999).

[46] J. Feldbrugge and N. Turok, Gravitational lensing of binary systems in wave optics, arXiv:2008.01154.

[47] J. Feldbrugge, Multi-plane lensing in wave optics, Mon. Not. R. Astron. Soc. **520,** 2995 (2023).

[48] A. G. Suvorov, Wave-optical effects in the microlensing of continuous gravitational waves by star clusters, Astrophys. J. **930,** 13 (2022).

[49] M. Serone, G. Spada, and G. Villadoro, The power of perturbation theory, J. High Energy Phys. 05 (2017) 056.

[50] S. Birrer *et al.*, Lenstronomy II: A gravitational lensing software ecosystem, J. Open Source Software **6,** 3283 (2021).

[51] G. Pagano, O. A. Hannuksela, and T. G. F. Li, lensingGW: A Python package for lensing of gravitational waves, Astron. Astrophys. **643,** A167 (2020).

[52] J. Wagner and X. Er, Plasma lensing in comparison to gravitational lensing—Formalism and degeneracies, arXiv: 2006.16263.

[53] S. Savastano, F. Vernizzi, and M. Zumalacárregui, Through the lens of Sgr A*: Identifying strongly lensed continuous gravitational waves beyond the Einstein radius, arXiv:2212 .14697.

[54] C. Dalang, G. Cusin, and M. Lagos, Polarization distortions of lensed gravitational waves, Phys. Rev. D **105,** 024005 (2022).

[55] M. A. Oancea, R. Stiskalek, and M. Zumalacárregui, From the gates of the abyss: Frequency- and polarization-dependent lensing of gravitational waves in strong gravitational fields, arXiv:2209.06459.

[56] M. A. Oancea, R. Stiskalek, and M. Zumalacárregui, Probing general relativistic spin-orbit coupling with gravitational waves from hierarchical triple systems, arXiv:2307.01903.

[57] J. M. Ezquiaga and M. Zumalacárregui, Gravitational wave lensing beyond general relativity: Birefringence, echoes and shadows, Phys. Rev. D **102,** 124048 (2020).

[58] C. Dalang, P. Fleury, and L. Lombriser, Scalar and tensor gravitational waves, Phys. Rev. D **103,** 064075 (2021).

[59] A. K.-W. Chung and T. G. F. Li, Lensing of gravitational waves as a novel probe of graviton mass, Phys. Rev. D **104,** 124060 (2021).

[60] S. Goyal, A. Vijaykumar, J. M. Ezquiaga, and M. Zumalacarregui, Probing lens-induced gravitational-wave birefringence as a test of general relativity, Phys. Rev. D **108,** 024052 (2023).